THE ASTROPHYSICAL JOURNAL, 457:211–227, 1996 January 20

THE GAS AND DUST ABUNDANCES OF DIFFUSE HALO CLOUDS IN THE MILKY WAY[1]

KENNETH R. SEMBACH[2,3] AND BLAIR D. SAVAGE[4]
Received 1995 May 15; accepted 1995 August 1

ABSTRACT

We present Goddard High-Resolution Spectrograph observations of the interstellar Mg II, Si II, P II, S II, Mn II, Cr II, Fe II, Ni II, Zn II, and Ge II lines toward HD 116852, a star at -1.3 kpc from the Galactic plane and a distance of 4.8 kpc in the direction $l = 304.^{\circ}9$, $b = -16.^{\circ}1$. The intermediate-resolution (FWHM $\approx$ 11–18 km s^{-1}) observations of these species have S/N $\approx$ 30–90. The high-resolution (FWHM = 3.5 km s^{-1}) observations of Mn II and Fe II reveal a rich interstellar velocity structure extending from ≈ -70 to $+35$ km s^{-1}. The velocity separation of the absorption components caused by differential Galactic rotation allows us to study the abundances of halo clouds below the Sagittarius and Norma spiral arms. We find that the gas-phase abundances of Mg, Si, S, Mn, Cr, Fe, and Ni relative to Zn in the HD 116852 halo clouds are very similar to those of clouds in the low halo ($0.3 \leq |z| \leq 1.5$ kpc) toward high-latitude stars in the solar neighborhood. There is a progression toward increasing gas-phase abundance from the Galactic disk to halo. For the entire cloud sample, the average logarithmic gas-phase abundance ratios relative to solar abundance ratios are [Mg/Zn] = -0.52, [Si/Zn] = -0.26, [S/Zn] = -0.05, [Mn/Zn] = -0.61, [Cr/Zn] = -0.51, [Fe/Zn] = -0.64, and [Ni/Zn] = -0.84. Since Zn is not depleted in the warm neutral gas, these abundance values should be the same as [X/H]. *There are no systematic differences in these abundances for halo clouds with galactocentric distances* $\approx$7–10 kpc. We find that dust grains contain approximately 70% of the Mg, 45% of the Si, and 77% of the Fe in the halo clouds. The small variation in the halo cloud abundances strongly supports the idea that the cores of the dust grains are resilient and difficult to destroy completely by the processes that circulate gas from the disk to the halo. The gas- and dust-phase abundance patterns in the halo clouds are consistent with more severe grain destruction in the clouds at greater distances from the plane. We calculate (Mg + Fe)/Si = 3.26 ± 0.64 in the dust grains if solar abundances are used as references and (Mg + Fe)/Si = 3.91 ± 0.64 if B-star reference abundances are used. These ratios imply that there must be grains composed of Fe-oxides, or perhaps pure Fe, in the halo clouds. Since pure Fe grains are destroyed much more rapidly than silicates behind fast shocks, we favor silicates and oxides as the likely constituents of grain material in the halo clouds.

Subject headings: dust, extinction — Galaxy: halo — ISM: abundances — ISM: clouds — stars: individual (HD 116852) — ultraviolet: ISM

1. INTRODUCTION

During the past few years we have been using the Goddard High-Resolution Spectrograph (GHRS) aboard the *Hubble Space Telescope* (*HST*) to study the physical conditions and elemental abundances in halo clouds toward distant stars. Many of the ultraviolet absorption-line studies we have so far performed have been tailored to determine the physical conditions and kinematics of highly ionized gas in the hot interstellar medium (Savage, Sembach, & Cardelli 1994; Savage & Sembach 1994; Sembach & Savage 1994, hereafter Paper I), but ultraviolet spectroscopy is also essential for determining the gas-phase abundances within neutral and weakly ionized interstellar gas, since the resonance lines of many astrophysically important ions have wavelengths between 1150 and 3000 Å. The high-resolution and high signal-to-noise capabilities of the GHRS make it possible to obtain precise column densities of many atomic species and to explore both the gas- and dust-phase elemental abundances within the interstellar medium (ISM) in great detail (Sofia, Cardelli, & Savage 1994; Cardelli, Sembach, & Savage 1995). Our investigations of Milky Way halo gas complement interstellar research being conducted with the GHRS by Spitzer & Fitzpatrick (1992, 1993, 1995).

In this paper we report the results of a study of elemental abundances in halo clouds toward the O9 III star HD 116852. The star lies at a distance of 4.8 kpc in the direction $l = 304.^{\circ}9$, $b = -16.^{\circ}1$ (see Paper I). The line-of-sight velocity gradient caused by differential rotation of the Galaxy in this direction is ≈ -10 km s^{-1} kpc^{-1}, which makes it feasible to investigate how the interstellar absorption signature, and hence the composition of the gas, changes along the sight line. The GHRS measurements of HD 116852 permit us to study halo gas extending out to -1.3 kpc from the Galactic plane and thus compare the composition of gas situated below spiral arms (Sagittarius and Norma) along the sight line to that of gas in the solar neighborhood determined through GHRS studies of high-latitude halo stars.

We describe the GHRS observations of HD 116852 in § 2 and present descriptions of the high-resolution velocity structure and sight line properties in § 3. Section 4 contains information about the column densities of the interstellar ions observed and estimates of the gas-phase abundances in the

[1] Based on observations obtained with the Goddard High-Resolution Spectrograph on the NASA/ESA *Hubble Space Telescope*, obtained at the Space Telescope Science Institute, which is operated by the Association of Universities for Research in Astronomy, Inc., under NASA contract NAS5-26555.

[2] Center for Space Research, 6-216, Massachusetts Institute of Technology, 77 Massachusetts Avenue, Cambridge, MA 02139; sembach@sundoggie.mit.edu.

[3] Hubble Fellow.

[4] Washburn Observatory, University of Wisconsin-Madison, 475 N. Charter Street, Madison, WI 53706; savage@madraf.astro.wisc.edu.

TABLE 1

GHRS OBSERVATIONS OF HD 116852[a]

HST Archive Identification	Grating	Resolution[b] FWHM (km s^{-1})	Wavelength (Å)	Exposure Time[c] (s)	Species Observed
Z15F010AT.....	G200M	13.3	2024.5–2065.1	1382.4	Mg I, Cr II, Zn II
Z15F010CT.....	G270M	11.0	2574.8–2622.9	512.0	Mn II, Fe II
Z15F010FT.....	Ech-B	3.5	2596.5–2609.3	1075.2	Mn II, Fe II
Z15F010GT.....	Ech-B	3.5	2253.8–2265.7	1638.4	Fe II

[a] Additional GHRS UV observations are listed in Table 1 of Paper I. Ground-based optical observations of Ca II and Na I can be found in Sembach et al. 1993.

[b] All spectra were obtained with the small (0.″25 × 0.″25) science aperture. The resulting Gaussian instrumental spread functions have the indicated full widths at half-maximum intensity.

[c] On-spectrum exposure time. These times represent about 89% of the total exposure time, as ≈11% of the total time was spent measuring the background near the spectrum.

halo clouds. In § 5 we compare these halo cloud abundances to those for clouds in the solar neighborhood and discuss the composition of the interstellar grains in the halo of the Galaxy. Sections 6 and 7 contain discussions of how the results for HD 116852 and the halo cloud sight lines relate to the destructive processing of dust as it is transported into Galactic halo.

2. OBSERVATIONS AND REDUCTION

We obtained the GHRS observations listed in Table 1 to determine the velocity structure and column densities of Mg I, Mn II, Cr II, Fe II, and Zn II in the halo clouds toward HD 116852. The observations, illustrated in Figure 1, consisted of two high-resolution (Ech-B; FWHM ≈ 3.5 km s^{-1}) measurements of the 2260 Å and 2600 Å spectral regions and two intermediate-resolution (G200M, G270M; FWHM ≈ 11–13 km s^{-1}) observations of the 2025–2065 Å and 2575–2620 Å spectral regions. We observed HD 116852 with the light from the star in the small (0.″25 × 0.″25) science aperture of the spectrograph, which yields spectra with Gaussian instrumental spread functions with the values of FWHM listed above. All science observations were obtained with the FP-Split, comb-addition, and Doppler compensation procedures enabled. We removed scattered light from the echelle observations according to the method outlined by Cardelli, Ebbets, & Savage (1993). The characteristics of the GHRS and its in-orbit performance are discussed by Brandt et al. (1994).

Small velocity shifts (<1 diode) applied to each spectrum were necessary to align the interstellar features with the low ion lines presented in Paper I. We estimate that this low ion "bootstrap" results in relative velocity uncertainties of less than 4 km s^{-1} for the intermediate-resolution data and less than 2 km s^{-1} for the echelle data. We converted the heliocentric to LSR velocities using the relation $v_{\rm LSR} = v_{\rm helio} - 6.4$ km s^{-1}.

Continuum normalized versions of the high-resolution (Ech-B) interstellar data for the HD 116852 sight line are plotted as a function of LSR velocity in the left panel of Figure 2 together with the Na I D and Ca II K profiles obtained by Sembach, Danks, & Savage (1993) using the Coudé Echelle Spectrograph at the European Southern Observatory. The optical data have a resolution of ≈4.5 km s^{-1} (FWHM) and signal-to-noise ratios (S/N) ≈ 90 (Na I) and ≈40 (Ca II). At the bottom of the panel we show the G270M spectrum of the Fe II λ2600 line for comparison with the Ech-B observations. In the right panel of Figure 2 we illustrate an assortment of the intermediate-resolution profiles for the sight line. Table 2

TABLE 2

EQUIVALENT WIDTHS

Ion	IP (eV)[a] (x^{i-1})	IP (eV)[a] (x^{i})	λ[b] (Å)	f-Value[c]	$W_\lambda \pm 1\sigma$ (mÅ)	Velocity Range (km s^{-1})	S/N[d]
Mg I	...	7.65	2026.477	1.154 (−1)	82.3 ± 4.7	−25 to +35	49
Cr II.....	6.77	16.50	2056.254	1.052 (−1)	93.8 ± 8.5	−85 to +55	48
			2062.234	7.796 (−2)	74.3 ± 8.6	−85 to +25	45
Mn II.....	7.44	15.64	2576.877	3.508 (−1)	300.3 ± 5.8	−85 to +55	58
			2594.499	2.710 (−1)	263.2 ± 6.1	−85 to +55	56
			2606.462	1.927 (−1)	227.2 ± 6.3	−85 to +55	54
					232.5 ± 5.8[e]	−85 to +55	33
Fe II.....	7.87	16.18	2260.780	2.440 (−3)	150.0 ± 4.3[e]	−85 to +55	43
			2586.650	6.840 (−2)	672.2 ± 3.2	−85 to +55	67
			2600.173	2.130 (−1)	760.0 ± 3.5	−85 to +55	61
					765.0 ± 3.2[e]	−85 to +55	38
Zn II	9.39	17.96	2026.136	4.886 (−1)	187.9 ± 6.9	−85 to +25	49
			2062.664	2.564 (−1)	110.5 ± 7.7	−45 to +55	45

[a] Creation and destruction ionization potentials from Moore 1970.

[b] Rest vacuum wavelengths listed by Morton 1991.

[c] Fe II *f*-values from Cardelli & Savage 1995. Zn II and Cr II *f*-values from Bergeson & Lawler 1993. Mg I and Mn II *f*-values from Morton 1991.

[d] Point-to-point S/N in the continuum near the line.

[e] These equivalent width values are from Ech-B measurements. All others are from intermediate-resolution measurements.

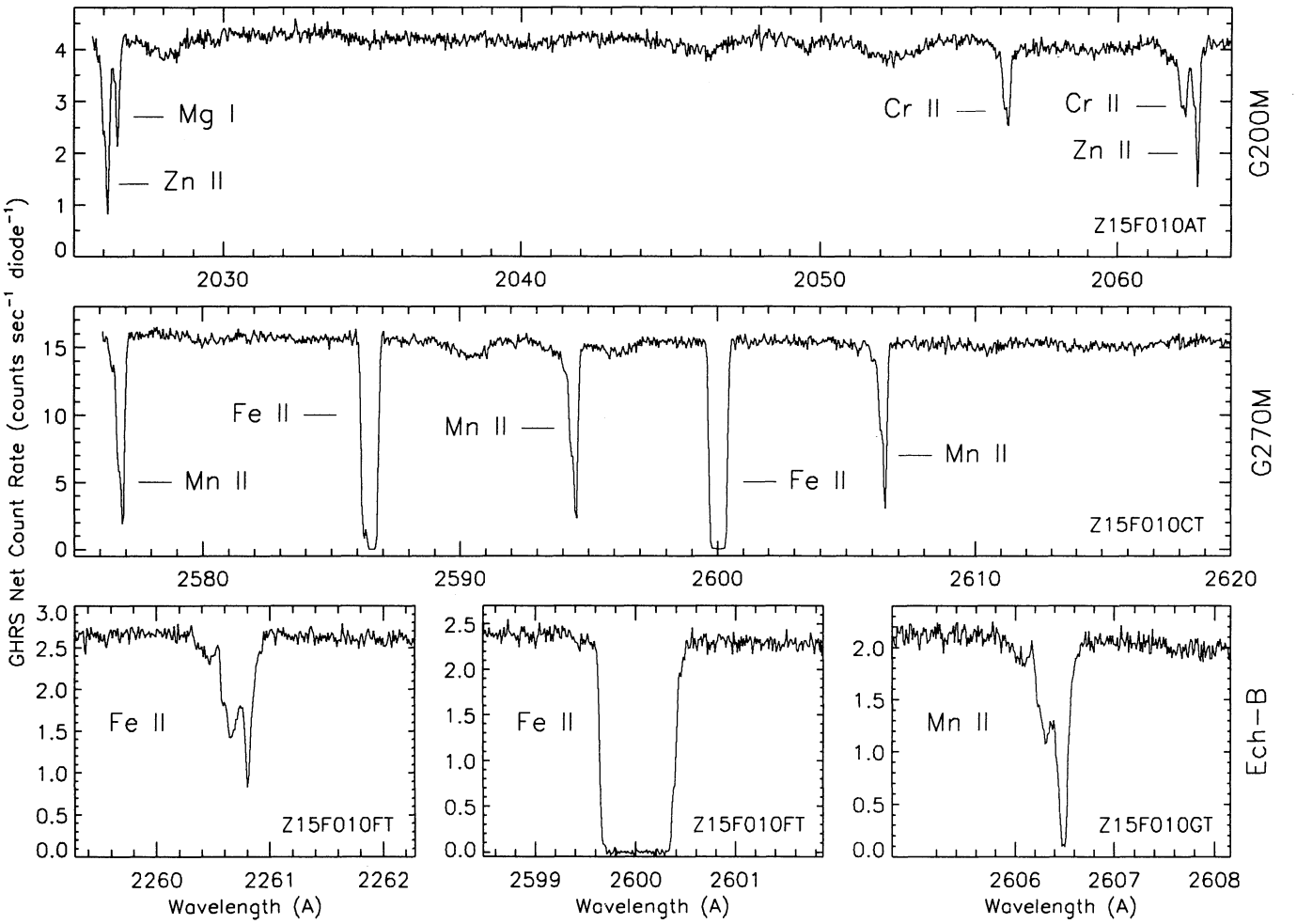

FIG. 1.—GHRS net count rate vs. wavelength for the intermediate-resolution (G200M, G270M) and high-resolution (Ech-B) observations of HD 116852 obtained for this study. Information about the observations is provided in Table 1. The equivalent width for each line identified in the figure is listed in Table 2. The intermediate-resolution data have S/N ≈ 45–70, and the echelle data have S/N ≈ 35. The abscissae of the three panels containing the Ech-B data are expanded by about a factor of 4 compared to the upper two panels.

provides a summary of the total equivalent widths of the lines detected in the spectra listed in Table 1. Paper I contains the equivalent widths for the remaining lines along with a description of the continuum fitting procedure.

In subsequent sections of this paper we draw upon additional low-ionization interstellar line profiles displayed and analyzed in Paper I. A representative sampling of these profiles for several species (e.g., Ni II, S II, and Si II) is shown in the right panel of Figure 2. We use these previous GHRS observations in combination with our new measurements to determine relative abundances in the halo clouds along the sight line, and we compare them to the absorption profiles of Al III and Si IV to provide information about the ionization of the gas.

3. VELOCITY STRUCTURE

The high-resolution observations of Na I, Ca II, Mn II, and Fe II shown in the left panel of Figure 2 reveal a rich interstellar velocity structure that is partially discernible in the intermediate-resolution observations in the right panel. The weak line Ca II, Mn II, and Fe II profiles shown have a similar velocity structure over the −70 to +35 km s^{-1} velocity range covered by the strong Fe II λ2600 line. The large spread in absorption velocities is due in large part to Galactic rotation effects along the HD 116852 sight line. The top left panel of Figure 2 contains a plot of the Galactic H I rotation curve for the HD 116852 direction. The heavy solid line shows the LSR velocity versus distance relationship derived by Clemens (1985) assuming a solar Galactocentric distance of 8.5 kpc and solar speed of 220 km s^{-1}. We have made the reasonable assumption that halo gas out to the distance of the star corotates with the underlying disk gas (see Lockman 1984). The heavy short-dashed lines show the typical scatter introduced in the relationship by an H I cloud-to-cloud velocity dispersion of ≈8 km s^{-1} (Falgarone & Lequeux 1973). A portion of the high-resolution Ca II profile overplotted in this panel shows the complexity of the absorption structure at negative velocities. We now discuss in more detail the velocity structure along the sight line and describe the absorption characteristics revealed by these high-resolution observations before undertaking an analysis of the intermediate-resolution data in § 4.

3.1. *Component Fits*

A minimum of eight distinct components contribute to the absorption along the HD 116852 sight line. We arrive at this

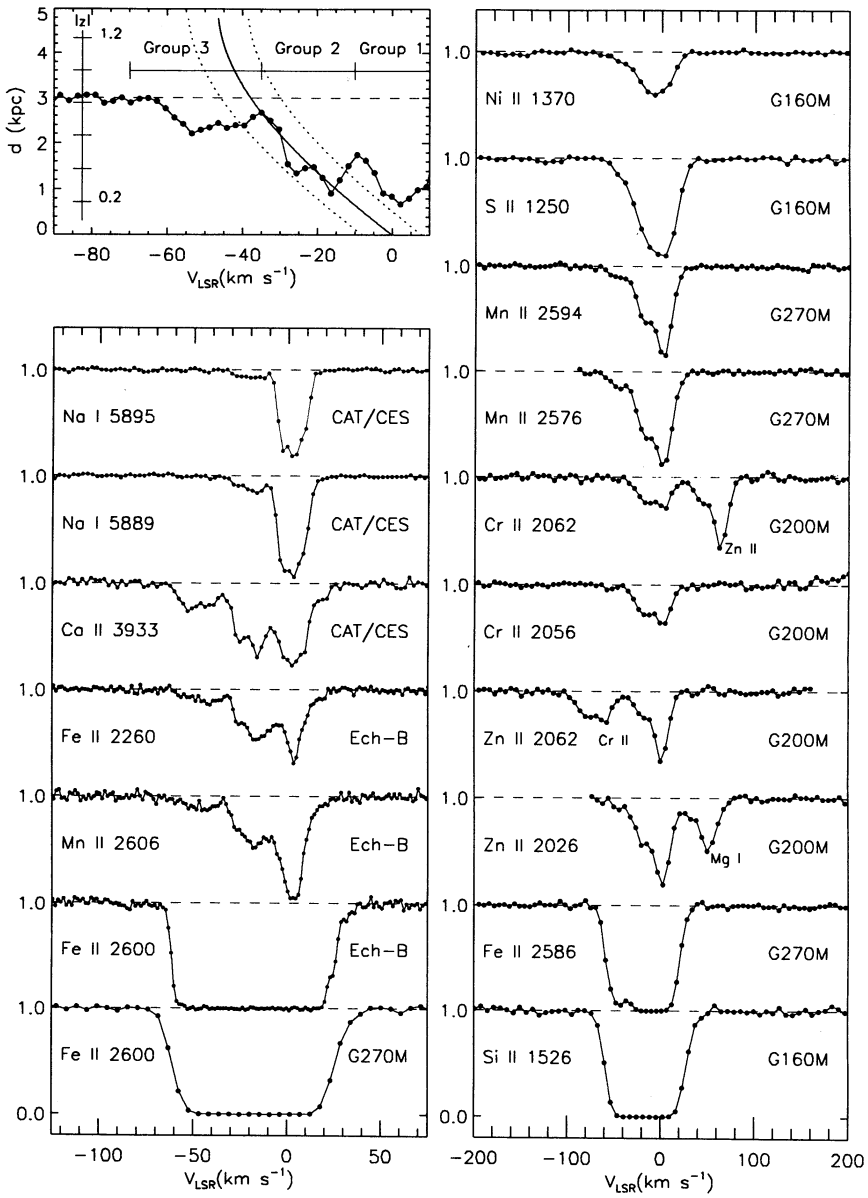

FIG. 2.—Continuum normalized intensity vs. LSR velocity for the interstellar lines in the spectrum of HD 116852. In several cases, more than one species is detectable in the velocity interval illustrated: Cr II λ2062 with Zn II λ2062 at $v_{LSR} = -62$ km s^{-1}, Zn II λ2062 with Cr II λ2062 at $v_{LSR} = +62$ km s^{-1}, and Mg I λ2026 with Zn II λ2026 at $v_{LSR} = +50$ km s^{-1}. The stellar continuum for each line was approximated by a low-order polynomial fitted to the regions on either side of the line (see Paper I). For HD 116852, $v_{LSR} = v_{helio} - 6.4$ km s^{-1}, assuming the Sun is moving at 16.5 km s^{-1} in the direction $l = 53°$, $b = +25°$ (Mihalas & Binney 1981). The small panel in the upper left shows an expanded view of the normalized Ca II λ3933 profile toward HD 116852 and the relationship between distance (d and z) and velocity for the sight line assuming halo gas corotates with the underlying disk gas.

conclusion by combining the velocity information in the high-resolution Ca II, Mn II, and Fe II profiles in the following manner: We fitted the Fe II λ2260 profile with several components and allowed their central velocities ($\langle v_i \rangle$), widths (b_i), and column densities (N_i) to vary using the component fitting procedure described by Sembach et al. (1993). Then we fixed the velocities of these components for the Mn II λ2606 and Ca II λ3933 lines during a similar fitting procedure in which only the b_i and N_i varied. We repeated this process by adding additional components until all three profiles could be fitted well, as indicated by a goodness-of-fit parameter near unity (i.e., $\chi^2_\nu \approx 1$). The eight components required to produce acceptable fits with χ^2_ν(Fe II) = 1.0, χ^2_ν(Mn II) = 1.3, and χ^2_ν(Ca II) = 1.1 are listed in Table 3. For comparison, Table 3 also contains component fit results for the Na I doublet profiles, though there is no detectable Na I at the highest negative velocities covered by the Ca II, Mn II, and Fe II profiles ($v_{LSR} \leq -35$ km s^{-1}).

We have grouped the fit components listed in Table 3 into the three intervals (groups 1–3) indicated on the distance versus velocity plot in Figure 2. Since these groups can be distinguished, but not velocity resolved, in many of the intermediate-resolution profiles, they provide convenient reference points for discussing the absorption. Fortunately, these divisions in velocity are also scientifically interesting; the velocities of component groups 2 and 3 span a large fraction of

TABLE 3

INTERSTELLAR VELOCITY STRUCTURE TOWARD HD 116852[a]

Component	$\langle v_{LSR} \rangle$ (km s^{-1})	Fe II λ2260		Mn II λ2606		Ca II λ3933		Na I λλ5889, 5895	
		b (km s^{-1})	N (cm^{-2})	b (km s^{-1})	N (cm^{-2})	b (km s^{-1})	N (cm^{-2})	b (km s^{-1})	N (cm^{-2})
3b	−55	4.7 ± 1.8	3.6 ± 1.0 (13)	10.8 ± 3.0	1.0 ± 0.3 (12)	5.2 ± 0.6	3.8 ± 0.6 (11)		
3a	−42	8.1 ± 2.2	1.4 ± 0.3 (14)	8.1 ± 2.2	1.2 ± 0.4 (12)	8.2 ± 1.3	5.4 ± 1.0 (11)		< 5.0 (10)
2b	−27	1.6 ± 0.5	8.0 ± 3.5 (13)	3.7 ± 0.7	1.4 ± 0.4 (12)	3.5 ± 0.2	9.4 ± 1.2 (11)	5.3 ± 1.4	1.1 ± 0.3 (11)
2a	−17	8.0 ± 0.6	6.2 ± 0.5 (14)	7.7 ± 1.0	6.8 ± 0.9 (12)	4.3 ± 0.2	1.5 ± 0.1 (12)	4.6 ± 1.4	1.4 ± 0.5 (11)
1d	−3	8.3 ± 2.1	3.8 ± 1.0 (14)	5.2 ± 0.6	5.8 ± 0.8 (12)	5.3 ± 0.3	1.2 ± 0.2 (12)	3.0 ± 0.1	1.1 ± 0.1 (12)
1c	+3	2.3 ± 0.3	3.2 ± 0.6 (14)	3.5 ± 0.2	1.9 ± 0.2 (13)	5.3 ± 0.3	1.9 ± 0.2 (12)	5.7 ± 0.1	3.1 ± 0.2 (12)
1b	+8	4.2 ± 1.4	1.6 ± 0.5 (14)	4.7 ± 0.5	3.0 ± 0.5 (12)	1.1 ± 0.2	6.0 ± 1.7 (11)	...	...
1a	+18	3.3 ± 1.2	4.0 ± 1.9 (13)	5.1 ± 1.7	6.5 ± 2.6 (11)	4.8 ± 1.1	2.7 ± 0.7 (11)	...	3.0 ± 1.0 (10)

[a] Component fit results for the high-resolution interstellar Fe II, Mn II, Ca II, and Na I data for HD 116852. The component velocities are set by the Fe II λ2260 profile. For a Gaussian profile, FWHM = 1.667b.

the 1.3 kpc the sight line extends away from the Galactic plane (see inset scale in Fig. 2 for z-distance). The absorption associated with groups 2 and 3 is also relatively weak, which allows accurate column densities to be derived.

We show the fit results for Ca II, Mn II, and Fe II in Figure 3, where we have plotted the apparent column density profiles constructed from the high-resolution data. A continuum normalized absorption profile, $I(v)$, for a line having a rest wavelength, λ (in Å), and an oscillator strength, f, is related to an apparent column density profile, $N_a(v)$ [atoms cm^{-2} (km s^{-1})$^{-1}$], through the equation

$$N_a(v) = \frac{m_e c/\pi e^2}{f\lambda}\,\tau_a(v) = 3.768 \times 10^{14}\,\frac{\ln[-I(v)]}{f\lambda(\text{Å})}\,. \quad (1)$$

$N_a(v)$ is an *apparent* column density per unit velocity because the original absorption line is viewed through an instrumental spread function having a finite resolution and saturation effects may be important. Savage & Sembach (1991) have shown that such a conversion results in a valid, instrumentally blurred version of the true $N(v)$ profile provided it does not contain a significant amount of unresolved saturated structure (see § 4 for a discussion of this issue). The value in constructing such profiles is that the column density information at any velocity is immediately accessible and available for comparison with other species.

The heavy solid lines overplotted on the data in Figure 3 are the cumulative profiles resulting from the fitting process described above, and the thin solid lines show the individual components. We have blurred the fits shown in Figure 3 to the appropriate instrumental resolution for each species. The vertical tick marks above the Ca II K profile indicate the velocities of the individual components listed in Table 3. We now briefly described the general properties of each grouping of components.

Component group 1.—The four components comprising this group ($v_{LSR} > -10$ km s^{-1}) are heavily blended, and therefore the details of the absorption structure are more uncertain than they are for the components at higher negative velocities. The strong, narrow component (1c) near +3 km s^{-1} dominates the absorption in this component group. The gas within this group must have relatively high densities, since fine-structure excited levels of C I are detected near zero velocity (see Paper I). We measure Mg I absorption with a logarithmic column density of log N(Mg I) = 13.25 ± 0.05 based on direct integration of the 2026 Å line. The N(Mg I)/N(Na I) ratio of ≈4 ± 2 is typical for cool (T ∼ 100 K) diffuse clouds (Pettini et al. 1977). Component 1a at $v_{LSR} \approx +18$ km s^{-1} has a peculiar velocity about twice that expected for cool H I clouds in the disk (Falgarone & Lequeux 1973; Spitzer 1978), and the N(Ca II)/N(Na I) ratio of 10 is more characteristic of warm gas than the ratios of <1 found for the remainder of the group 1 absorption (see Sembach & Danks 1994). The N(Fe II)/N(Mn II) ratio of ≈62 in component 1a is also several times larger than the ratio of ≈17 deduced for the strong component at +3 km s^{-1}.

Component group 2.—This grouping (-35 km s$^{-1} \leq v_{LSR} \leq -10$ km s^{-1}) consists of two components separated by about 10 km s^{-1}. Both components contain Na I, although the absorption is weak. The ratios of Ca II to Na I in the two components are similar to the value of 10 found for component 1a. Of the two components, 2a is stronger and has N(Mg I)/N(Na I) ≥ 20. This ratio, which is based on a comparison of the $N_a(v)$ profiles for Mg I and Na I, is indicative of dielectronic recombination occurring in warm ($T \geq 7000$ K) gas; note that the temperature of the gas may actually be considerably higher than this limit (see Pettini et al. 1977). For the Galactic rotation curve given by Clemens (1985), the $-35 \leq v_{LSR} \leq -10$ km s^{-1} velocity interval corresponds to a kinematic distance interval of $0.7 \leq d \leq 2.7$ kpc, which in turn corresponds to distances (z) of $0.2 \leq |z| \leq 0.7$ kpc below the Galactic plane (see Fig. 2).

Component group 3.—This grouping (-70 km s$^{-1} \leq v_{LSR} \leq -35$ km s^{-1}) is composed of two components at −55 and −42 km s^{-1}. Figure 3 reveals an interesting reversal in the strengths of the lines from Fe II and Mn II to Ca II. This change in relative strengths of the ions is most likely due to grain disruption but may also be affected partly by changes in the ionization of the clouds (see § 3.2). Since the star is located near the sight line tangent point ($d_{tp} \approx 5$ kpc), velocities more extreme than ≈ -47 km s^{-1} are not expected for this sight line. Therefore, the absorption within this interval probably represents either gas at z-distances of $0.7 \leq |z| \leq 1.3$ kpc or gas at lower z-distances with large peculiar velocities.

The N(Fe II)/N(Mn II) = 80 ± 23 ratio in the group 3 components is similar to the value of 85 ± 12 found for the group 2 components and is about a factor of 2.5 larger than the ratio of 32 ± 13 for group 1. This strongly suggests the elemental abundances of groups 2 and 3 differ substantially from those for low-velocity gas confined to the Galactic disk. The great strengths of many of the group 1 absorption lines prevent a thorough analysis of the sight line abundances at low velocities, but we shall see shortly that the halo clouds of groups 2 and 3 do indeed have gas-phase abundances more nearly solar than those of diffuse disk clouds.

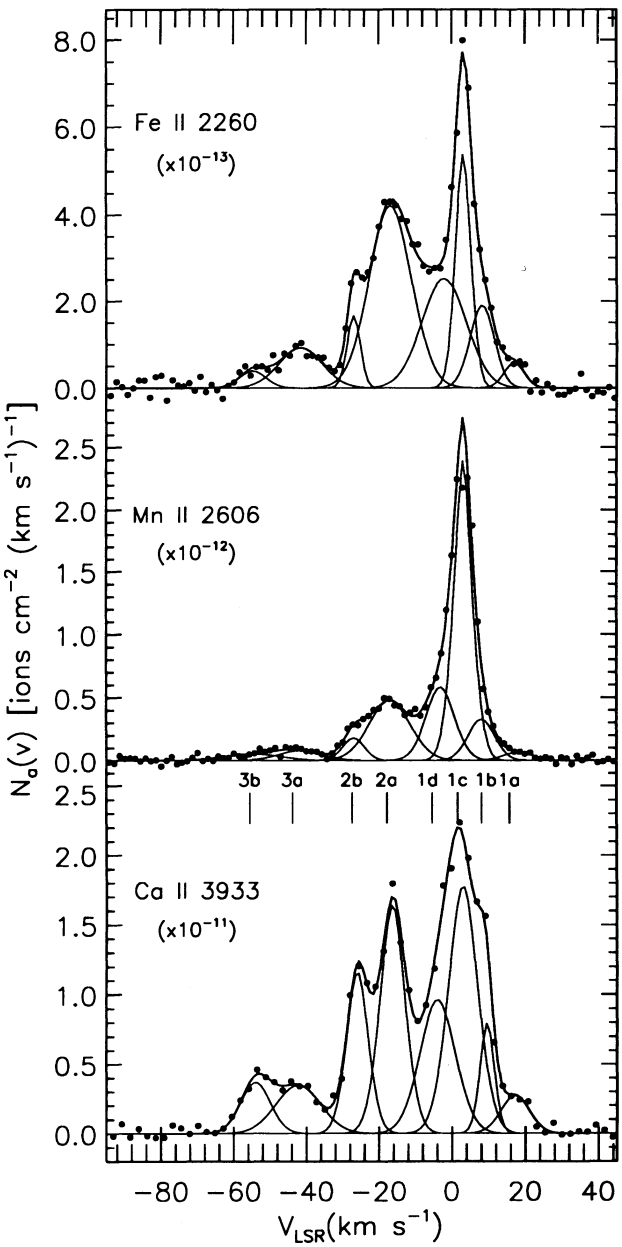

FIG. 3.—Apparent column density per unit velocity vs. LSR velocity for the high-resolution Fe II, Mn II, and Ca II data toward HD 116852 (*filled circles*). The values of $N_a(v)$ are calculated as discussed in § 3 of the text. The heavy solid line in each panel shows the instrumentally blurred composite profile derived by simultaneously fitting the three absorption line profiles. The individual components numbered 1a–3b in the bottom panel are shown as thin solid lines in each panel; they have been blurred to the instrumental resolution appropriate for each species. The parameters describing these components can be found in Table 3.

3.2. *Sight Line Overview*

HD 116852 lies at a distance of 4.8 kpc ($z = -1.3$ kpc) in the interarm region beyond the Sagittarius-Carina and Norma-Centaurus spiral arms near $l = 305°$. The Sagittarius spiral arm lies at a distance of approximately 1.5–2.0 kpc in this direction and has a velocity of -20 to -30 km s^{-1}. The Norma arm is located at a distance of about 3.5 kpc and has velocities of -30 to -50 km s^{-1} in the Galactic disk (Bok 1971; Courtès et al. 1970; Rickard 1974). The arms are well defined by the H II regions they contain (Courtès 1972), but they are less readily distinguished in H I surveys (Kerr et al. 1986). The HD 116852 sight line passes under the Sagittarius and Norma spiral arms at z-distances of about -500 and -1000 pc, respectively. H I 21 cm emission at the latitude of the star ($b = -16.°1$) remains quite strong out to ≈ -30 km s^{-1} but drops quickly to a value of $< 2 \times 10^{18}$ [atoms cm^{-2} (km s^{-1})$^{-1}$)] by $v_{LSR} \approx -40$ km s^{-1} (Colomb, Gil, & Morras 1976; Kerr et al. 1986). This H I emission level is consistent with the *velocity-integrated* H I column densities of $N(\text{H I})_{\text{Group 2}} = 10^{20}$ cm^{-2} and $N(\text{H I})_{\text{Group 3}} = 2 \times 10^{19}$ cm^{-2} inferred from the Zn II and S II lines at negative velocities (see § 4).

CO maps of the sky reveal molecular emission in the disk near $l = 305°$ extending from 0 to -50 km s^{-1} (Dame et al. 1987). The Chamaeleon molecular cloud complex located in the direction of HD 116852 at a distance of about 200 pc has a CO velocity of $\approx +4$ km s^{-1} (Dame et al. 1987) and is probably the site of the C I fine-structure lines detected near zero velocity in Paper I.

Additional information about the relationship of gas in the disk and low halo in this direction is available in the form of high-resolution Na I and Ca II data. In Figure 4 we show the interstellar Na I D_2 and Ca II K absorption profiles toward HD 116852 and five disk stars in the same general longitudinal direction as HD 116852. The dashed vertical lines in the figure delineate the velocities of the three component groups discussed in § 3.1. Several aspects of this figure are noteworthy:

1. The HD 116852 Ca II profile reveals a stronger recovery to the continuum near $v_{LSR} \approx -10$ km s^{-1} than the disk sight lines having strong absorption at this velocity. This is within 5 km s^{-1} of the velocity at which the HD 116852 Al III absorption is a maximum, suggesting that there could be ionized gas in the halo at this velocity. In Paper I we tentatively identified the Al III absorption peak with gas over the Sagittarius spiral arm, but it is also possible this is ionized gas in the interarm region between the Sagittarius arm and the Sun.
2. The group 2 Na I absorption toward HD 116852 is much weaker than it is toward the disk stars. The HD 116852 sight line samples a more diffuse ISM below the Sagittarius spiral arm at these velocities than the disk star sight lines passing through the arm.
3. The amount of Ca II toward the disk stars at the velocities of component group 3 is small compared to the amount toward HD 116852, except for HD 113012. There appears to be no absorption in this interval toward the disk stars until $d \approx 3$–4 kpc. The strong Ca II component near $v_{LSR} \approx -50$ km s^{-1} toward HD 113012 is probably the result of distant disk gas in the Norma spiral arm. Toward HD 113012 the Ca II feature has strong associated Na I absorption (as expected for disk gas), but there is no detectable Na I absorption toward HD 116852 at this velocity. The high ion lines of Si IV and C IV toward HD 116852 show modest column density increases near -50 km s^{-1} that may be related to ionized disk gas in the Norma spiral arm (see Paper I).

These observations lead us to the conclusion that there is some gas associated with spiral arms influencing the HD 116852 absorption in component groups 2 and 3 even though the sight line crosses the arms at large (≥ 0.5 kpc) $|z|$-distances. Whether this absorption arises in gas circulating between the disk and halo or in vertical extensions of the Sagittarius and Norma spiral arms in the disk remains to be determined.

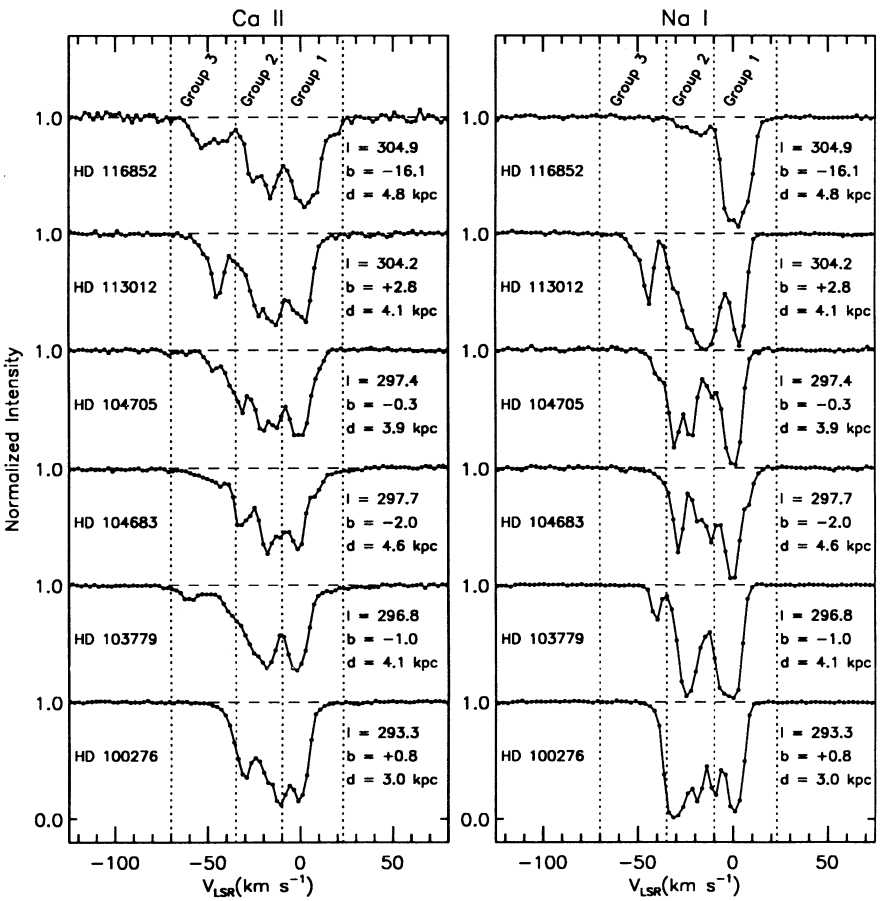

FIG. 4.—Normalized intensity vs. LSR velocity for the interstellar Na I D_2 and Ca II K profiles toward HD 116852 and five disk stars in the same longitudinal direction. Note the large amount of Ca II at the velocities of the group 3 components toward HD 116852. There is little absorption toward the disk stars at this velocity. Note also the relatively weak Na I absorption in the group 2 components toward HD 116852 compared to the disk sight lines. Some of the absorption in the HD 116852 group 2 and 3 components is associated with spiral arms along the sight line (see text for details).

Further descriptions of the sight line and the properties of ionized disk and halo gas in this direction can be found in Paper I and Sembach (1994).

4. COLUMN DENSITIES AND GAS-PHASE ABUNDANCES IN THE HD 116852 HALO CLOUDS

4.1. *Apparent Column Density Profiles and Component Blending*

We used the formulation of $N_a(v)$ in equation (1) to construct the low ion apparent column density profiles shown in Figure 5. Each panel contains a comparison of two lines having strengths that vary by approximately a factor of 2 (except Ni II, for which only one line was observed). The error bars on each point indicate the 1 σ uncertainties caused by Poisson noise fluctuations in the data and continuum placement uncertainties. There is generally excellent agreement between the two profiles of each species for velocities more negative than about -15 km s^{-1}. Mg II, S II, and Cr II contain a small amount of unresolved saturated structure between ≈ -25 to -10 km s^{-1}, since the weak-line profiles (*solid circles*) imply larger values of $N_a(v)$ than the strong-line profiles (*open circles*), and for this reason we focus our interpretation upon only the weak-line profiles. The single line of Ni II observed (λ1370) may contain a small amount ($\sim 10\%$) of unresolved saturated structure at low velocities. The apparent optical depth of the line is between those of the Mg II λ1239 and S II λ1250 lines, but the resolution is slightly better ($\approx$16 vs. 18 km s^{-1}). It is unlikely the $-70 \leq v_{LSR} \leq -35$ km s^{-1} portion of the λ1370 line is affected by unresolved saturated structure. For the remaining ions, the good agreement of the $N_a(v)$ profiles indicates that there is no substantial unresolved saturated structure within the profiles.

The intermediate-resolution profiles shown in Figure 5 do not afford the opportunity for the detailed profile fitting possible for the echelle observations. However, the lack of unresolved saturated structure at velocities outside the strong, low-velocity line cores implies that column densities can be obtained by integrating these profiles over the velocity ranges $-35 \leq v_{LSR} \leq -10$ km s^{-1} (group 2) and $-70 \leq v_{LSR} - 35$ km s^{-1} (group 3). These two ranges correspond to the velocities spanned by the groups 2 and 3 components defined by the high-resolution data. We list the integrated column densities of the lines over the three velocity ranges in Table 4.

When using intermediate-resolution data to derive column densities and abundance ratios over specific velocity ranges by integrating apparent column density profiles, it is important to assess whether "spillover" from neighboring absorption caused by the finite resolution of the spectrograph affects the quality of the results. In Table 5 we list the column densities obtained by integrating the echelle and intermediate-resolution Mn II λ2606 data over the $-35 \leq v_{LSR} \leq -10$ km

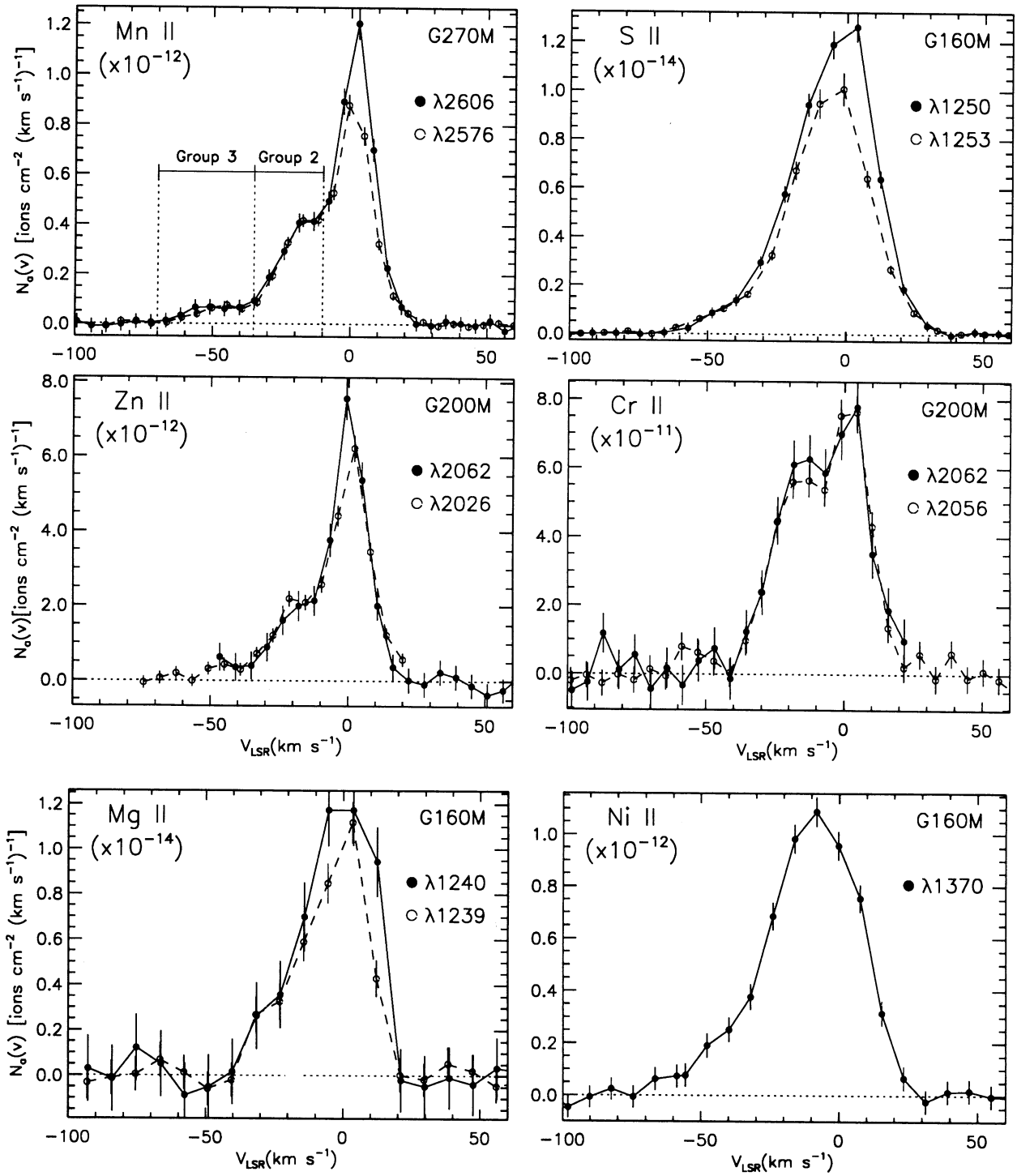

FIG. 5.—Apparent column density profiles for the HD 116852 intermediate-resolution interstellar data. The $N_a(v)$ values derived from two lines for each species are shown (except Ni II, for which only one line was measured). The good agreement between the profiles within each species for velocities less than about -10 km s^{-1} indicates that reliable column densities can be obtained by integrating the profiles at these velocities. In the few cases in which the profiles do diverge, we use the weak line results (*filled circles*), since these are less affected by unresolved saturated structure. The upper left panel for Mn II shows the two velocity ranges considered in this study. Integrated column densities and abundance ratios for each velocity range are listed in Table 4.

TABLE 4

COLUMN DENSITIES AND GAS-PHASE ABUNDANCES[a]

Ion (X) (1)	$A(X)_\odot$[c] (2)	$-\le v_{LSR} \le -35$ km s^{-1} (Group 3)[b] (-1σ) (3)	log N_a (4)	$(+1\sigma)$ (5)	[X/Zn] (6)	$-35 \le v_{LSR} \le -10$ km s^{-1} (Group 2)[b] (-1σ) (7)	log N_a (8)	$(+1\sigma)$ (9)	[X/Zn] (10)	$v_{LSR} > -10$ km s^{-1} (Group 1)[b] (-1σ) (11)	log N_a (12)	$(+1\sigma)$ (13)
H I	12.00	...	19.26[d]	...	...	...	19.99[d]	...	...	...	20.90[e]	...
Mg II.....	7.58	...	<14.64	...	<-0.28	15.08	15.13	15.17	$-0.47^{+0.05}_{-0.06}$	...	>15.44	...
Si II.....	7.55	...	>14.39	...	>-0.49	...	>14.56	...	>-1.00	...	...	...
P II	5.57	...	...	...	...	13.49	13.62	13.72	$+0.04^{+0.10}_{-0.13}$	14.00	14.06	14.12
S II	7.27	14.43	14.47	14.51	$-0.13^{+0.09}_{-0.12}$	15.23	15.25	15.27	$-0.03^{+0.03}_{-0.04}$	...	>15.40	...
Mn II.....	5.53	12.25	12.30	12.34	$-0.56^{+0.10}_{-0.12}$	12.89	12.91	12.92	$-0.63^{+0.03}_{-0.04}$	13.41	13.43	13.45
Cr II.....	5.68	...	<12.54	...	<-0.47	13.03	13.06	13.09	$-0.63^{+0.04}_{-0.04}$	13.18	13.22	13.25
Fe II.....	7.51	14.14	14.18	14.23	$-0.66^{+0.09}_{-0.12}$	14.83	14.84	14.85	$-0.68^{+0.03}_{-0.03}$	14.94	14.96	14.98
Ni II.....	6.25	12.72	12.78	12.83	$-0.80^{+0.10}_{-0.13}$	13.32	13.34	13.36	$-0.92^{+0.03}_{-0.04}$	...	>13.33	...
Zn II	4.65	11.87	11.98	12.06	...	12.63	12.66	12.69	...	13.04	13.06	13.08
Ge II	3.63	...	...	...	...	11.42	11.59	11.71	$-0.05^{+0.12}_{-0.17}$	11.96	12.03	12.09

[a] Integrated apparent column densities and abundance ratios relative to Zn for the low ionization species detected in this study and in Paper I. The apparent column density profiles are shown in Figs. 3 and 5. The gas-phase abundance ratio of element X relative to Zn is given by [X/Zn] = log [N(X II)/N(Zn II)] − [$A(X)_\odot$ − $A(Zn)_\odot$].

[b] Assuming corotation with gas in the underlying disk, the indicated velocity intervals correspond to the following distance intervals.
group 1: $0.0 \le d \le 0.7$ kpc; $0.0 \le |z| \le 0.2$ kpc; $8.5 \ge R_g \ge 8.1$ kpc.
group 2: $0.7 \le d \le 2.7$ kpc; $0.2 \le |z| \le 0.7$ kpc; $8.1 \ge R_g \ge 7.3$ kpc.
group 3: $2.7 \le d \le 4.8$ kpc; $0.7 \le |z| \le 1.3$ kpc; $7.3 \ge R_g \ge 7.0$ kpc.

[c] Logarithmic solar system meteoritic abundances given by Anders & Grevesse 1989, where $A(X)_\odot = \log(X/H) + 12$.

[d] The neutral hydrogen column density inferred from the listed values of N(Zn II) and N(S II), assuming that these species are not depleted onto dust grains and do not have significant H II region contributions (see § 4).

[e] The neutral hydrogen column density inferred from the total value of log N(H I) = 20.96 (Diplas & Savage 1994) less the values of log N(H I) for groups 2 and 3 (see note d).

s^{-1} and $-70 \le v_{LSR} \le -35$ km s^{-1} velocity ranges, and we compare these values with those obtained by summing the column densities of the individual groups 2 and 3 components obtained by the fitting procedure described in § 3.1. For the Mn II G270M data, we obtained fit results by forcing the $\langle v_i \rangle$ and b_i values to be equal to those found for the higher resolution echelle observations; only the optical depths of each component were allowed to vary to minimize the residuals in the fit. The values of log N_a derived for the Ech-B and G270M data using equation (1) and the total values of log N found from the fitting procedure for each interval agree to within the listed errors. Therefore, we conclude that integrating the intermediate-resolution $N_a(v)$ profiles over the two velocity intervals is essentially equivalent to decomposing the profiles and summing the column densities of the individual components as was done for the echelle data.

TABLE 5

COLUMN DENSITY BLENDING: THE Mn II VELOCITY DISTRIBUTION

Effective Resolution (km s^{-1})	$-70 \le v_{LSR} \le -35$ km s^{-1} (-1σ)	log N_a	$(+1\sigma)$	$-35 \le v_{LSR} \le -10$ km s^{-1} (-1σ)	log N_a)	$(+1\sigma)$
Ech-B: Measured and Fit Results[a]						
3.5 Integration	12.25	12.30	12.34	12.89	12.91	12.92
3.5 Component Fit	12.21	12.34	12.43	12.86	12.91	12.96
G270M: Measured and Fit Results[b]						
11.0 Integration.....	12.26	12.32	12.37	12.91	12.92	12.93
11.0 Component Fit.....	12.21	12.29	12.35	12.88	12.90	12.92
Additional Spread Function Width Results[c]						
3.5	12.25	12.30	12.34	12.89	12.91	12.92
11.0	12.26	12.31	12.35	12.91	12.92	12.93
13.0	12.27	12.32	12.36	12.92	12.93	12.94
15.0	12.28	12.33	12.37	12.93	12.94	12.95
18.0	12.30	12.34	12.38	12.94	12.95	12.96

[a] Ech-B: Integrated apparent column densities measured from the high-resolution Mn II λ2606 profile shown in Fig. 3 and determined from the group 2 and 3 components found from the fitting process described in § 3.

[b] G270M: Same as note a, except for the G270M Mn II data.

[c] Apparent column densities for several effective resolutions spanning the range of the spread function widths used for the observations in this study. Note that the values for each interval are within about 10% (0.04 dex) of those found by direct integration of the Ech-B profile.

Next, we explore how differences in the velocity widths of the instrumental spread functions affect the component blending and measured column densities. Starting with the Mn II echelle profile, we blurred the data to successively poorer resolutions in $N_a(v)$ space. The values of log N_a for effective resolutions of 3.5, 11.0, 13.0, 15.0, and 18.0 km s^{-1} are listed in Table 5. There is a systematic trend to slightly overestimate the column density in each interval as the resolution worsens. Absorption from the group 1 components mixes with the group 2 components, and group 2 absorption mixes with the group 3 components. However, the net effect of this blurring on the column densities derived for each interval, even at the poorest resolution of the data obtained for this study ($\approx$18 km s^{-1} near 1250 Å), is likely to be less than about 0.04 dex (10%).

4.2. *Gas-Phase Abundances*

The logarithmic gas-phase abundance of element X in an H I region is given by the following equation:

$$\left[\frac{\mathrm{X}}{\mathrm{H}}\right] = \log\left[\frac{N(\mathrm{X\ II})}{N(\mathrm{H\ I})}\right] - \log\left(\frac{\mathrm{X}}{\mathrm{H}}\right)_c , \qquad (2)$$

where $(\mathrm{X/H})_c$ is the cosmic ratio of X to H. We want to examine the gas-phase abundances over specific velocity (i.e., distance) intervals but know only the total sight line H I column density determined from the damped Lyα absorption line at 1216 Å [N(H I) = 9.1 $\times$ 10^{20} cm^{-2}; Diplas & Savage 1994]. We circumvent this limitation by substituting Zn for H in the above equation and noting that Zn II is the dominant stage for Zn in H I regions. Measurements of Zn II generally provide reliable estimates of the Zn abundance in low-density gas because Zn is not easily locked into dust grains. For diffuse gas sight lines, log (Zn/H) is within $\approx$ 0.2 dex of the solar ratio (Sembach et al. 1995).[5] We list values of [X/Zn] for Mg, Si, P, S, Mn, Cr, Fe, Ni, and Ge in Table 4 for the $-70 \le v_{\mathrm{LSR}} \le -35$ km s^{-1} (group 3) and $-35 \le v_{\mathrm{LSR}} \le -10$ km s^{-1} (group 2) velocity ranges. Phosphorus, sulfur, and germanium have gas-phase abundances (relative to Zn) within about 10% of their solar values; magnesium, silicon, maganese, chromium, and iron have gas-phase abundances within about a factor of 5 of solar; and nickel has a gas-phase abundance within about a factor of 10 of solar.

In calculating the values of [X/Zn], we have adopted the "solar" abundances derived from meteoritic data by Anders & Grevesse (1989) as cosmic reference abundances. Column (2) of Table 4 gives these values in the standard logarithmic system where $A(\mathrm{X})_\odot$ = log (X/H) + 12. Solar abundances derived from photospheric and meteoritic data generally agree to within about 10% (0.04 dex). Those elements having well-determined meteoritic abundances differing substantially from the photospheric values (e.g., Mn, Fe, and Ge) are discussed by Anders & Grevesse (1989). It is important to note that various lines of evidence suggest that the solar abundances adopted differ for some elements from those in young, main-sequence B stars and gaseous nebulae (see discussions in Gies & Lambert 1992 and Sofia et al. 1994). Among the elements we consider here, main-sequence B-star abundance measurements exist for Si, S, and Fe with $A(\mathrm{X})_{\mathrm{B\text{-}star}}$ = 7.58, 7.21, and 7.72, respectively (Gies & Lambert 1992). Therefore, $A(\mathrm{X})_{\mathrm{B\text{-}star}} - A(\mathrm{X})_\odot$ = +0.03, −0.06, and +0.21 for Si, S, and Fe. The large difference for Fe (0.21 dex, or a factor of 1.62) provides a good example of the reference abundance problem. In the following discussions we will derive gas-phase abundances based upon the solar references listed in Table 4, but we will occasionally discuss how our conclusions change if we switch to B-star abundances.

[5] The value of [Zn/H] $\ge$ −0.4 for the entire sight line represents a lower limit to the amount of Zn in the gas phase in the group 2 and 3 components, since the gas-phase abundance of Zn is density dependent and the densest gas along the sight line occurs near zero velocity as indicated by the C I fine-structure lines.

4.3. *The Effects of Ionization on Derived Abundances*

The singly ionized species illustrated in Figure 5 are the dominant-ion states of these elements in H I regions, but the ions illustrated may also exist in H II regions, since their second ionization potentials range from 15.0 eV (Mg II) to 23.3 eV (S II). In the previous section we derived gas-phase abundances assuming these species arise solely within H I regions along the sight line. However, there is evidence to suggest some of the gas along the HD 116852 sight line is at least partially ionized. In Paper I we show that moderately ionized has traced by Al III (18.8–28.8 eV) absorbs at velocities from $v_{\mathrm{LSR}} \approx -70$ to +20 km s^{-1} and highly ionized gas traced by Si IV (33.5–45.1 eV), C IV (47.9–64.5 eV), and N V (77.4–97.9 eV) absorbs at velocities from $v_{\mathrm{LSR}} \approx -100$ to +50 km s^{-1}. Therefore, these ionized species have velocities similar to those of the low-ionization species within the halo clouds along the sight line. Measurements of the diffuse Hα background (Reynolds 1993, and references therein) suggest that much of the diffuse ionized gas (DIG) observed in directions out of the Galactic plane is warm ($T \approx$ 8000 K), has a relatively large filling factor ($\approx$20%–25%), and has an average electron density of $\approx$0.1 cm^{-3}. Absorption-line studies of other halo lines show that some halo electrons may be clumped in warm H I halo clouds having a filling factor comparable to that of the DIG (see Spitzer & Fitzpatrick 1993).

To see the range of effects ionization may have on the gas-phase abundances along the HD 116852 sight line, we consider two cases. The first, in which all the singly ionized gas arises in H I regions, was discussed in § 4.2 and will serve as a zero-order approximation for comparison with the second, in which the singly ionized gas arises primarily in H II regions. The suitable range of test cases to use for the situation involving H II regions is set by the observed ratio of N(Si II)/N(Si IV) in the halo clouds. This ratio depends strongly upon the properties of the H II regions intersected by the sight line; the ratio decreases as the ionization parameter (the ratio of ionizing photon to particle densities) increases. For an extended, low-density path such as the HD 116852 sight line, most of the ionized gas contributions to the singly ionized species probably arise in the diffuse ionized gas (DIG) observed by Reynolds (1993).

We use the DIG ionization calculations recently published by Dömgorgen & Mathis (1994) to estimate the ionization corrections necessary to account for the relative amounts of singly ionized species in the diffuse ionized gas. Since much of the Si IV along the sight line probably arises by collisional ionization (see below), we make a conservative (generous) estimate of DIG contributions to the amount of Si IV along the sight line by adopting the results for a DIG model that predicts a volume average Si ion abundance ratio $[N(\mathrm{Si\ II})/N(\mathrm{Si\ IV})]_{\mathrm{DIG}} \approx 3$, which is less than the observed ratio $[N(\mathrm{Si\ II})/N(\mathrm{Si\ IV})]_{\mathrm{obs}} > 20$ in the group 2 and 3 components (see Paper I). This DIG model also has the nice property that $[N(\mathrm{H\ II})/N(\mathrm{H\ I})]_{\mathrm{DIG}} \approx 15$, which agrees with the ratio of

ionized to neutral hydrogen for the diffuse Hα background found by Reynolds (1993).

An additional consistency check on the appropriateness of this DIG model as a limiting case for the HD 116852 halo clouds can be made by estimating the relative amounts of singly and doubly ionized Al in them. GHRS measures of Al III yield log N(Al III) = 12.94 ± 0.02 and 12.42 ± 0.04 in component groups 2 and 3 (Paper I). Unfortunately, we do not have GHRS measurements of Al II absorption, but we can make an estimate of N(Al II) in the group 3 components using the HD 116852 interstellar Al II λ1670 profile observed by the *International Ultraviolet Explorer* (*IUE*) satellite. The Al II profile is strong and unresolved at the 25 km s^{-1} resolution of the *IUE*, so we are able to derive only a lower limit of log N(Al II) > 12.8 (2 σ) for the group 3 velocity range in the wings of the observed absorption line (see Sembach & Savage 1992 for *IUE* data processing and analysis information). As expected, the ratio of singly to doubly ionized Al in the DIG model, $[N(\text{Al II})/N(\text{Al III})]_{\text{DIG}} \approx 1.6$, is smaller than the lower limit $[N(\text{Al II})/N(\text{Al III})]_{\text{obs}} > 2.4$ imposed by the observations for the group 3 clouds.

We now estimate the gas-phase abundances derived from observations of the singly ionized species if they arise completely in the DIG. We calculate $[\text{X/S}]_{\text{DIG}}$ rather than $[\text{X/Zn}]_{\text{DIG}}$, since the DIG models focus upon only the most abundant elements [i.e., $A(\text{X})_{\odot} \geq 6.0$] and do not explicitly include Zn. Using S in place of Zn does not appreciably alter our conclusions because the halo cloud column densities in Table 4 indicate log N(S II)/N(Zn II) ≈ log $(\text{S/Zn})_{\odot}$, and neither element is readily incorporated into dust grains (see Harris & Mas Hesse 1986; Sembach et al. 1995). If all the singly ionized gas arises in the DIG, then the gas-phase abundances in Table 4 derived under the assumption of neutral gas conditions must be corrected: $[\text{X/S}]_{\text{DIG}} = [\text{X/S}]_{\text{H I}} + \Delta_{\text{X/S}}$, where $\Delta_{\text{X/S}} = +0.08, -0.20, +0.17$, and $+0.15$ dex for Mg, Si, Fe, and Ni, respectively.

While the properties of the ionizing regions at the velocities of the HD 116852 halo clouds may fluctuate about those described by the DIG model discussed above, the values of [X/Zn] listed in Table 4 should be accurate to within ≈0.15 dex even if all the singly ionized species observed arise in the DIG. Cardelli et al. (1995) arrived at a similar conclusion when considering the ionization conditions along the inner Galaxy HD 167756 sight line for a comparable set of elements. H I 21 cm emission observations and pulsar dispersion measures of $N(e^-)$ toward globular clusters (Reynolds 1991) indicate that N(H II)N(H I) ≈ 0.37 in the Galactic halo. If this ratio of ionized to neutral hydrogen holds for the HD 116852 sight line, then the ionization corrections, $\Delta_{\text{X/S}}$, are probably closer to 0.06 dex than 0.15 dex. It is also important to note that $\Delta_{\text{X/Zn}}$ is probably less than $\Delta_{\text{X/S}}$ in most instances, since Zn has first and second ionization potentials more similar to those of the other elements studied than does S and should therefore behave more similarly to these other elements in diffuse ionized gas situations (although dielectronic and radiative recombination coefficients can also have a significant effect on ionic abundance). It would be desirable to include Zn in the elemental inventories of the DIG models to determine $\Delta_{\text{X/Zn}}$ directly.

So far we have considered photoionization as the sole source of ionization along the sight line. For the diffuse ionized gas, this seems reasonable, since the only known source capable of providing the energy required to keep the gas ionized in a steady state is photons from O-stars (Miller & Cox 1993; Reynolds 1993). The relative quantities of Si IV, C IV, and N V at the velocities of the halo clouds along the HD 116852 sight line suggest that the higher ionization species are produced by collisional ionization in gas with $T \sim 10^5$ K (see Paper I). At these temperatures, most elements are in their second, third, or fourth stages of ionization, and contributions of the singly ionized stage to the elemental abundance are minor. For example, in collisional ionization equilibrium at 10^5 K, N(Si II)/N(Si) ≈ 1.5 × 10^{-4} and N(Si II)/N(Si IV) ≈ 2.9 × 10^{-3} (Sutherland & Dopita 1993). Therefore, we expect very little singly ionized gas to exist in the regions containing the highly ionized species produced by collisional ionization. Note that the possible production of Si IV by collisions at high temperatures supports our assumption that the true *photon* ionization parameter is not as high as the one assumed for the DIG H II region calculations.

4.4. *The Effects of Abundance Gradients in the Galaxy*

It is also important to consider how our choice of solar abundances as the cosmic reference standard for interstellar clouds influences our conclusions about the abundances in the clouds at large line-of-sight and z-distances. The HD 116852 sight line probes gas over Galactocentric radii between R_g = 7.0–8.5 kpc and z-distances up to 1.3 kpc. In the disk, the value of [Fe/H] in stars does not change substantially over these Galactocentric radii (0.15 ± 0.32 dex; see Rana 1991), and other Fe-group elements (Cr, Mn, Ni, and Zn) show no systematic abundance trends relative to Fe over large metallicity ranges (i.e., ⟨[X/Fe]⟩ ≈ 0; Wheeler, Sneden, & Truran 1989). Therefore, we expect no Galactic abundance gradient contributions for these elements in the values of [X/Zn] in Table 4. From studies of H II regions, Shaver et al. (1983) measure an abundance gradient of ≈0.08 ± 0.02 dex kpc^{-1} for N and O, but more recent stellar abundance studies suggest that there is essentially no abundance gradient for C, N, O, Ne, Mg, Al, Si, S, or Fe within about 3 kpc of the solar circle (Fitzsimmons et al. 1990; Kilian-Motenbruck, Gehren, & Nissen 1994). We expect the differences in the abundance gradient contributions to [X/Zn] for these elements in the group 2 and 3 components to be less than the measurement errors of the data.

The stellar [Fe/H] ratio changes substantially as a function of distance from the Galactic plane and is expected to decrease by as much as ≈0.8 dex over the 1.3 kpc z-distance of HD 116852 (see Rana 1991, and references therein). This change in stellar [Fe/H] is due directly to the differences in the disk and halo stellar populations and probably does not reflect such large changes in the present-day interstellar gas metallicities, since turbulent motions of gas in the disk are adequate to sufficiently stir the ISM in the disk and populate the low halo with H I clouds (Lockman & Gehman 1991). Indeed, there seems to be a higher ratio of Fe to H at higher z-distances than found for many other low-ionization species (Edgar & Savage 1989). Increases in the gas-phase abundances of Fe-peak elements at large distances from the Galactic plane may be the result of Type I supernova explosions that enrich the high-z gas (van Steenberg & Shull 1988), though there has been no direct observational information that would favor this idea over the plausible alternative that refractory elements are liberated from dust grains as they are transported from the disk into the low halo by supernovae, radiation pressure, cloud-cloud interactions, or other processes.

We favor the cycling of material between the gas and dust phases of the ISM as the most likely source of variation

between the halo cloud abundances we observe toward HD 116852 and those normally found for disk gas (see also Spitzer & Fitzpatrick 1993, 1995; Cardelli et al. 1995). The fact that there is little variation between the abundances derived for the group 2 and group 3 halo clouds toward HD 116852 indicates that there are no strong trends in abundance ratios as a function of z or d over an appreciable fraction of the 4.8 kpc line. As we shall now show, this result applies to the much larger Galactocentric distance range covered when additional halo cloud sight lines are considered.

5. COMPARISONS WITH OTHER DIFFUSE CLOUD SIGHT LINES AND IMPLICATIONS FORTHE COMPOSITION OF INTERSTELLAR DUST GRAINS

The column density and abundance information available for the HD 116852 halo clouds provides a basis for comparison with other diffuse cloud sight lines in the disk and halo. In Table 6 we list the HD 116852 gas-phase abundances from Table 5 together with those for the diffuse clouds toward HD 18100, HD 36486 (μ Col), HD 93521, HD 149757 (ζ Oph), HD 149881, HD 167756, and 3C 273. For comparison with these sight lines, we also list the gas-phase abundances of the cool, diffuse disk clouds toward ξ Per and ζ Oph. The ζ Oph cloud is considerably denser than the warmer diffuse halo clouds ($n_H \approx$ 200–300 cm^{-3} vs. $\lesssim$1 cm^{-3}) and has a large molecular hydrogen fraction, $f(H_2) = 2N(H_2)/[N(H\ I) + 2N(H_2)] \approx 0.6$ (Savage, Cardelli, & Sofia 1992). For all sight lines, we have derived results from column densities converted into our preferred system of atomic constants and reference abundances. The notes to Table 6 contain the sources for the column density measurements and f-values.

Figure 6 is a graph of the results presented in Table 6. The elements on the abscissa of the plot have condensation

TABLE 6

GAS-PHASE ABUNDANCE COMPARISON[a]

SIGHT LINE	V_{LSR} (km s^{-1})	R_g (kpc)[b]	$\lvert z\rvert$ (kpc)[b]	[X/Zn] Mg	Si	S	Mn	Cr	Fe	Ni	Ti	
This Work												
HD 116852.....	−70 to −35 (group 3)	7.2–7.0	0.9–1.3	< −0.28	> −0.49	−0.13	−0.56	< −0.47	−0.66	−0.80	...	1
	−35 to −10 (group 2)	8.0–7.2	0.3–0.9	−0.47	> −1.00	−0.03	−0.63	−0.63	−0.68	−0.92	...	1
Warm, Diffuse Halo Clouds												
μ Col	+21 ($v_\odot$ = +41)	8.5–9.1	0.0–0.5	...	−0.22	−0.23	...	−0.38	−0.62	0.77	−0.35	2
HD 93521[c]	< −20 (fast)	8.6–8.9	0.3–1.5	−0.56	−0.25	−0.03	−0.60	...	−0.61	...	−0.90	3
HD 149881.....	−4	8.5–7.1	0.3–2.1?	...	−0.09	...	−0.47	−0.41	−0.58	...	...	3
	−14	8.5–7.1	0.3–2.1?	...	−0.29	...	−0.72	−0.61	−0.69	...	...	3
3C 273[d]	...	8.5–8.1	0.0–3.0	...	−0.47	+0.16:	−0.67	...	...	−0.81	...	4
Warm, Diffuse Disk + Halo Clouds												
HD 18100	−60 to +60	8.5–9.7	0.0–2.8	−0.62	−0.23	+0.03	−0.66	−0.72	−0.80	−1.15	...	5
HD 167756.....	≤ −10	6.7–4.7	0.4–0.8	−0.66	−0.28	...	...	−0.86	−0.98	...	...	6
	≥ +10	8.5–6.7	0.0–0.4	−0.59	−0.25	...	...	−0.88	−1.04	...	...	6
Warm, Diffuse Disk Clouds												
μ Col	+3 ($v_\odot$ = +23)	8.5–8.7	0.0–0.2?	−0.73	−0.35	+0.14	−0.85	−1.15	−1.24	1.44	−1.52	2
HD 93521[c]	> −20 (slow)	8.5–8.6	0.0–0.3	−0.85	−0.43	−0.03	−0.99	...	−1.19	...	−1.37	3
ζ Oph.....	−15 ($v_\odot$ = −27)	8.5–8.4	0.0	−0.90	−0.51	...	−0.87	−1.04	−1.19	−1.48	−1.31	7
Cool, Diffuse Disk Clouds												
ξ Per[e]	−1 to +14 (+5 ≤ $v_\odot$ ≤ +20)	8.5–9.0	0.0–0.1	−1.24	> −1.26	> −1.05	−1.32	−2.08	−2.09	−2.46	−2.59	8
ζ Oph[f]	−3 ($v_\odot$ = −15)	8.5–8.4	0.0	−1.56	−1.31	...	−1.45	−2.28	−2.27	−2.74	−3.02	7

[a] All values are referenced to the solar system meteoritic abundances given in Table 4 (from Anders & Grevesse 1989) and the oscillator strengths listed in Table 2 of this paper or Table 2 of Paper I, with the exception of Si II and Mg II, for which we adopt the f-values given by Dufton et al. (1983, 1992) and Sofia et al. (1994). The listed values of [X/Zn] have a 1 σ measurement error of $\approx$0.05 dex in most cases.

[b] *HD 18100*: This is a high-latitude direction ($b = -63°$) that may contain a small absorption contribution from the disk. There is little distance information for the clouds along this sight line. *μ Col*: The presence of molecules in the +23 km s^{-1} component indicates that the cloud is probably within 250 pc of the Galactic plane. *HD 93521*: Distance estimates based upon inspection of Fig. 4 in Danly 1989. *HD 116852*: Kinematic distance estimated as described in the text. *HD 149881*: Distances to these clouds are uncertain, but properties derived by Spitzer & Fitzpatrick 1995 suggest that they are not in the disk. *HD 167756*: Positive velocity components are not expected for this sight line. The > +10 km s^{-1} clouds are probably relatively nearby (i.e., d < 1–2 kpc, z < 400 pc). The negative velocity gas is probably a mix of disk and halo gas; kinematic distance estimates place the gas in the low halo. *3C 273*: This low-density direction has a latitude of +64° and probably samples mostly the warm ISM in the halo with little contribution from disk gas. The large negative velocity extents of the lines indicate that some of this gas is located in the low halo of the Galaxy (see Savage et al. 1993). The upper limit of z = 3 kpc is our estimate of a reasonable upper limit for the distance of these clouds from the Galactic plane.

[c] The HD 93521 abundance values are referenced to H, since the lines of Zn II were not observed. The solar abundance of S suggests that there probably is little depletion of Zn in these clouds.

[d] The 3C 273 values are referenced to H, assuming log N(H) = 20.22 from observations of the H I Lyα absorption (Savage et al. 1993). The S value is uncertain owing to the need for a large saturation correction.

[e] The ξ Per values are referenced to H assuming log N(H) = 21.30, since Zn appears to have a subsolar abundance.

[f] The ζ Oph values for the −15 km s^{-1} component are referenced to H, since the Zn lines are very strong and saturated. For this component, [Zn/H] ≥ −0.8, assuming log N(H) = 21.12.

REFERENCES.—(1) This paper. (2) Sofia, Savage, & Cordelli 1993. (3) Spitzer & Fitzpatrick 1993, 1995. (4) Savage et al. 1993. (5) Savage & Sembach 1995. (6) Cardelli et al. 1995. (7) Savage et al. 1992, Cardelli et al. 1994, Sofia et al. 1994. (8) Cardelli et al. 1991.

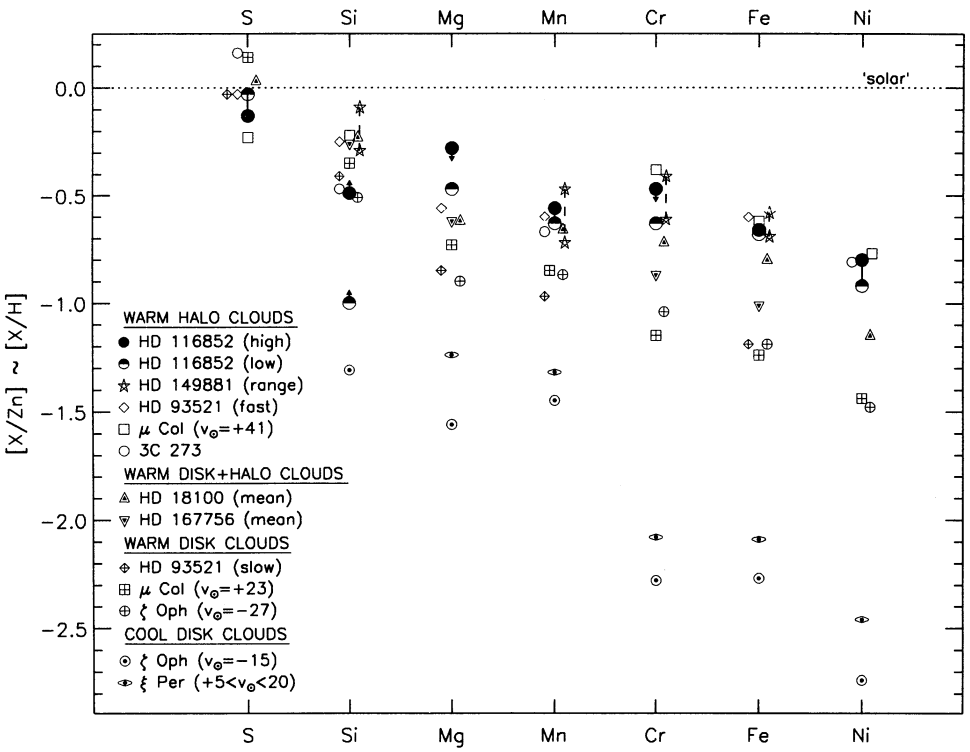

FIG. 6.—A comparison of the gas-phase abundances in the halo clouds toward HD 116852 with the abundances in other diffuse clouds in the disk and halo. The data for this figure are contained in Table 6, and the legend in the lower left identifies each sight line. Values for the cool ($T \approx 56$ K; Savage et al. 1977), diffuse cloud toward ζ Oph are shown for comparison with the other values. Approximate Galactocentric and z-distances of the clouds are given in Table 6. The small variation in relative abundances for the warm halo clouds is remarkable.

temperatures[6] within about 150 K of each other, except S, for which T_c is about a factor of 2 lower. We have grouped the clouds according to their approximate location above the plane of the Galaxy: halo clouds ($|z| \geq 300$ pc), disk + halo clouds (contributions from both high and low z are probably present), and disk clouds ($|z| < 300$ pc). These diffuse clouds show a significant trend in their gas-phase abundance properties as a function of distance from the Galactic plane. The halo clouds in this sample have [Si/Zn], [Mg/Zn], [Mn/Zn], and [Fe/Zn] that are 0.2, 0.3, 0.3, and 0.6 dex greater (respectively) than the warm disk cloud values. The disk + halo cloud population has intermediate gas-phase abundances for all the ions studied. We note that the diffuse halo cloud results are similar to those found from a recent *IUE* study of the $+70$ km s^{-1} cloud toward HD 203664. The intermediate velocity cloud along that sight line is located between 200 and 1500 pc from the plane of the Milky Way (Little et al. 1994) and has [Mg/S] $= -0.30$, [Si/S] $= -0.43$, [Mn/S] $= -0.40$, and [Fe/S] $= -0.57$ (Sembach 1995).

The small spread in the sight line–to–sight line values for the halo clouds suggests that the halo cloud abundances, and perhaps physical properties, are quite uniform over the Galactocentric radii sampled ($R_g \approx 7$–10 kpc). We have listed the approximate Galactocentric radii and z-distances of the individual clouds in Table 6. Information about these distance estimates is contained in the notes following the table. The locations of interstellar clouds are often difficult to determine, so many of these estimates are simply limits imposed by the stellar distances. The kinematic distances established for the clouds toward HD 116852 are probably some of the best-determined distances in the table. The tightness of the halo cloud abundance relation in Figure 6 suggests that the HD 116852 clouds may be warm ($T \sim 6000$ K) like those toward HD 93521 and HD 203664 (Spitzer & Fitzpatrick 1993; Little et al. 1994; Sembach 1995), but further high-resolution UV and H I radio observations are needed to confirm this.

The upper envelope of abundances established by the halo clouds represents an abundance pattern closer to solar than do the average low density ($n_H \sim 0.3$ cm^{-3}) ISM values based on the *Copernicus* satellite abundance survey (Jenkins, Savage, & Spitzer 1986; Jenkins 1987). The low density ($n_H \sim 0.03$ cm^{-3}) values from Jenkins (1987) are similar to those shown in our Figure 5 for the warm disk clouds. These comments allow for changes in f-values, particularly for the lines of Mg II. The subsolar values of [X/Zn] found for most of the species we have observed clearly indicate the presence of dust in halo clouds. Average values and rms variations of [X/Zn] for the halo cloud sight lines illustrated in Figure 6 are listed in Table 7. We believe the halo cloud abundance pattern is revealing the base level depletions of elements in dust grains that have been stripped of their protective mantles down to their resistant cores. If this interpretation is correct, the observed gas-phase abundances can be used to determine the actual composition of those dust cores.

The dust-phase abundance of a species X relative to hydrogen, $(X/H)_d$, is given by

$$(X/H)_d = (X/H)_c - (X/H)_g , \quad (3)$$

[6] Defined to be the temperature at which half the atoms of an element condense out of a gas of solar composition. At a pressure of 0.1 mbar, the condensation temperatures of S and Fe are about 700 and 1350 K, respectively (Grossman 1975).

TABLE 7

HALO CLOUD ABUNDANCE SUMMARY[a]

Value	[Mg/Zn]	[Si/Zn]	[S/Zn]	(Mn/Zn]	[Cr/Zn]	[Fe/Zn]	[Ni/Zn]
Average.....	−0.52	−0.26	−0.05	−0.61	−0.51	−0.64	−0.84
Root mean square.....	<0.19	0.14	0.14	0.09	0.13	0.04	0.07

[a] Averages and rms variations for the diffuse halo cloud abundances listed in Table 6. The abundances are referenced to Zn. Since [Zn/H] ≈ 0.0 dex in diffuse neutral gas (Sembach et al. 1995), the values of [X/Zn] are probably very similar to [X/H].

where the subscripts d, c, and g refer to dust, cosmic, and gas abundances, respectively. In equation (3) we assume that the difference between the cosmic abundance and the observed gas-phase abundance exists in the dust. We have used the average values of [X/Zn] in Table 7 for the halo clouds to determine the values of $(X/H)_d$ listed in Table 8. For the calculation, we assume Zn is not depleted in the halo clouds: $(Zn/H)_g = (Zn/H)_c = (Zn/H)_\odot = 4.47 \times 10^{-8}$. In Table 8 we also list values of $(X/H)_g$ and $(X/H)_c$, which we assume to be equal to the solar ratio $(X/H)_\odot$, and $(X/Si)_d = (X/H)_d/(Si/H)_d$, which is the relative dust-phase abundance of element X compared to Si.

Among the elements we have studied, those most abundant in the dust are Mg, Si, and Fe. According to several theories of the composition of interstellar dust, silicates, various oxides, and metallic iron are likely primarily constituents of dust grain cores. For example, amorphous olivines [$(Mg, Fe)_2SiO_4$] and pyroxenes [$(Mg, Fe)SiO_3$] are preferred silicate grain candidates (Ossenkopf, Henning, & Mathis 1992), while Fe_2O_3, Fe_3O_4, and MgO are the preferred oxide candidates (Nuth & Hecht 1990; Fadeyev 1988). If the actual interstellar dust cores consisted of pure olivines or pure pyroxenes, we would expect to measure (Mg + Fe)/Si = 2.0 or 1.0, respectively. The fact that we observe (Mg + Fe)/Si = 3.26 ± 0.64 implies that besides the favored silicate cores there is probably a population of oxides and perhaps pure iron grains. The dust composition numbers given in Table 8 will change if alternate cosmic reference abundances are adopted. For example, if instead of using the solar values of (Fe/H) and (Si/H) we use B-star abundance reference values of $(Fe/H) = 5.25 \times 10^{-5}$ and $(Si/H) = 3.80 \times 10^{-5}$ (Gies & Lambert 1992), we find $(Fe/H)_d = 4.51 \times 10^{-5}$ and $(Si/H)_d = 1.85 \times 10^{-5}$, and (Mg + Fe)/Si increases to 3.91 ± 0.64.

The dust-phase abundances in Table 8 will also change if ionization corrections of the type derived in § 4.3 are important. While it is uncertain whether such corrections are necessary for the HD 116852 sight line, let alone the others compiled for this study, we can estimate their impact on our conclusions by assuming that the ionization conditions do not vary between sight lines. The corrections serve to decrease the gas-phase abundance estimates of Mg, Si, and Fe relative to H in Table 8. The net effect on the dust-phase abundances in Table 8 would be to increase them to $(Mg/H)_d = 3.75 \times 10^{-5}$, $(Si/H)_d = 3.37 \times 10^{-5}$, and $(Fe/H)_d = 3.08 \times 10^{-5}$. Referencing the elements to S rather than H does not alter the resulting value of (Mg + Fe)/Si ≈ 2, which is only marginally compatible with a pure silicate grain core composition and should probably be considered a lower limit, since the ionization corrections are likely to be smaller than calculated in § 4.3.

The uncertainties in the f-values used in the column density determinations leading to the interstellar results in Table 8 are generally small (<15%). However, for the Mg II λλ1239, 1240 lines we have adopted the Sofia et al. (1994) f-values, which are larger by a factor of 4.7 than those listed by Morton (1991).[7] If the Morton f-values are used, the value of $(Mg/H)_g$ in Table 8 would increase by a factor of 4.7 and exceed the solar reference abundance by a factor of 1.4, which would indicate that there is a negligible amount of Mg in the dust grains in these clouds [i.e., $(Mg/H)_d \approx 0$]. For solar abundances, this would imply that (Mg + Fe)/Si ≈ $(Fe/Si)_d$ = 1,56, and a pure (olivine + pyroxene) silicate composition for the grain cores would be possible. For B-star abundances, we find $(Fe/Si)_d = 2.37$, and our previous conclusions about the necessity for oxide and/or pure Fe grain cores apply. Although we favor the Sofia et al. (1994) Mg II f-values, it would be highly desirable to obtain new laboratory f-value measurements for this important doublet.

6. IMPLICATIONS FOR DUST PROCESSING IN THE WARM NEUTRAL ISM

6.1. *Dust Destruction by Shocks*

It is generally accepted that shocks are responsible for most of the dust grain destruction in the ISM (Draine & Salpeter 1979; Draine & McKee 1993, and references therein), and it is likely that supernovae are the primary generators of these shocks in the disk and halo of the Galaxy. Grains can also be

[7] Morton 1991 lists $f_{1239} = 2.68 \times 10^{-4}$ and $f_{1240} = 1.34 \times 10^{-4}$. Sofia et al. 1994 prefer $f_{1239} = 1.25 \times 10^{-3}$ and $f_{1240} = 6.25 \times 10^{-4}$ based on a comparison of the column densities from the Mg II λλ1240, 2800 doublets. Their analysis involves sight lines for which the Mg II λ2800 doublet lines are so strong they exhibit damping wings.

TABLE 8

GAS- AND DUST-PHASE ABUNDANCES FOR HALO CLOUDS[a]

Abundance	Mg	Si	S	Mn	Cr	Fe	Ni
$(X/H)_\odot$	3.89 (−5)	3.55 (−5)	1.86 (−5)	3.39 (−7)	4.79 (−7)	3.24 (−5)	1.78 (−6)
$(X/H)_g$.....	1.17 (−5)	1.95 (−5)	1.66 (−5)	8.32 (−8)	1.48 (−7)	7.41 (−6)	2.57 (−7)
$(X/H)_d$[b].....	2.72 (−5)	1.60 (−5)	2.02 (−6)	2.56 (−7)	3.31 (−7)	2.49 (−5)	1.52 (−6)
$(X/Si)_d$	1.70	1.00	0.13	0.016	0.021	1.56	0.095

[a] These abundance results are based upon the meteoritic solar abundances from Anders & Grevesse 1989. If the Gies & Lambert 1992 B-star reference abundances are adopted, the four entries for Fe become 5.25 (−5), 7.41 (−6), 4.51 (−5), and 2.44, and the four entries for Si become 3.80 (−5), 1.95 (−5), 1.85 (−5), and 1.00.

[b] We assume $(X/H)_d = (X/H)_\odot - (X/H)_g$.

destroyed partly in the photodissociation regions near hot stars (Buss et al. 1994), but these environments are much denser and have higher far-ultraviolet photon densities than the diffuse interstellar environments considered here. The thermalization of the supernova kinetic energy and betatron acceleration of grains in the post-shocked regions behind supernova blast waves lead to grain-grain collisions and sputtering (both thermal and nonthermal). These processes are most efficient in the warm, neutral interstellar medium having properties similar to those inferred for the diffuse clouds listed in Table 6 (see McKee 1989).

McKee et al. (1987) have presented detailed models of the grain destruction caused by passage of shocks through the warm, neutral medium (WNM) and find that magnetic fields, or gas pressure drops behind shocks, can lead to much less grain destruction than previously calculated (e.g., Seab & Shull 1983). For a shock velocity of 100 km s^{-1} and a magnetic field strength of 3 μG, they find that only $\approx$10%–15% of the silicate grains behind the shock are destroyed. Refinements in these calculations made by including partial vaporization of the grains (Tielens et al. 1994; Jones et al. 1994) suggest that grains survive longer than previously thought as a result of the reduced destructiveness of grain-grain collisions, although the larger sputtering yields used in the calculations offset this effect and lead to net destruction results similar to those of McKee et al. (1987). Only a few such shocks appear to be necessary to liberate enough material from grains to produce the diffuse halo cloud abundances we observe.

The lifetime of a grain in the WNM varies depending upon its composition and the frequency and severity of passing shocks. On average, this lifetime is expected to be $\sim 10^8$ yr for a silicate grain (perhaps as much as 10^9 yr if the grains are porous (fluffy) and/or continuously remantled in cold clouds; see Jones et al. 1994). The systematic changes in the gas-phase abundances of the elements shown in Figure 6 are consistent with a progressively more severe processing of the dust from disk to halo. The upper envelope of gas-phase abundances we find for the diffuse halo clouds in Table 6 may reflect the abundance pattern of grains that have been stripped of their protective mantles to reveal their cores; the mantling process must occur in relatively cold clouds, unlike the halo clouds studied here but perhaps like the -15 km s^{-1} cloud toward ζ Oph. It is significant that we do not see solar ratios of these elements for any of the sight lines yet studied, since it indicates that these cores contain most of the Si and Fe at large distances from the plane and are difficult to destroy completely.

Interestingly, the grain destruction models predict that pure Fe grains are far more easily destroyed by fast shocks than silicate grains because of both their higher velocities in the post-shocked gas and their higher mass densities (Jones et al. 1994; McKee et al. 1987). When combined with our conclusion that there must be another Fe-bearing population or component to the grain constituency besides silicate grains in the low halo, this prediction favors oxides as the likely additional carrier of the Fe in the halo cloud dust.

The very tight relationships in the abundance patterns for the halo clouds also imply that there is little regeneration of mantles at large z-distances. However, potential sites for grain regrowth may exist in the halo. Observations of early-type stars at large distances from the plane show that the stars probably formed in the halo (see Keenan 1986), and a possible origin in which gas compressed by shocks produced during cloud-cloud collisions leads to star formation has been proposed by Dyson & Hartquist (1983). The net effect of these star-formation episodes on dust grains in the clouds is unknown but could perhaps be revealed through spectroscopic analyses of such regions.

6.2. *Application to Supernova Remnant Studies*

Spatial correlations between the infrared emission from dust grains and X-ray emission from hot plasmas in supernova remnants (Arendt et al. 1990; Arendt, Dwek, & Leisawitz 1992) show that dust can exist in a wide range of astrophysical environments. A preliminary analysis of Diffuse X-Ray Spectrometer measurements of the line ratios of Si VIII and S VIII in the hot, X-ray–emitting gas in the local ISM are consistent with Si being depleted from the gas phase by as much as a factor of 10 relative to S (Edgar et al. 1993). The existence of dust in such environments is important because it alters the emergent flux and spectral shape of the radiation emitted by the plasma. Vancura et al. (1994) have recently studied the effect of elemental depletions and dust destruction on the infrared and X-ray emissions of dusty, nonradiative shocks. They find that a thorough consideration of the initial elemental gas-phase abundances and dynamic evolution of dust grains is important for determining the gas temperatures, shock velocities, and ages of supernova remnants such as the Cygnus Loop. The abundance pattern derived for the resilient grain cores in diffuse halo clouds may provide an important reference point for grain destruction and evolution considerations in such models attempting to predict the emergent spectrum of shocked gas in interstellar environments.

7. DUST AND GAS IN THE GALACTIC HALO

The observations contained herein present evidence for dust in the low halo of the Milky Way. Dust has been detected in the halos of galaxies through scattered light observations (Neff et al. 1994) and background galaxy counts (Zaritsky 1994). The subject of dust in the hot halos of galaxies and clusters has been reviewed recently by Dwek & Arendt (1992).

One possible mechanism for injecting grains into the halo is through the supernovae explosions in the disk that vent their energy and expel material into the halo. The high ion column density ratios along the HD 116852 sight line (Paper I) are consistent with their creation in a "Galactic fountain," which is a likely source of highly ionized gas at kiloparsec distances from the plane (Sembach & Savage 1992). Single supernovae probably do not contribute significantly to the movement of gas or dust into the low halo unless they can readily expand into a low-density interarm or halo region, and therefore multiple, coordinated supernova events are required to move gas and dust into the halo (see Spitzer 1990; McKee 1993). The initial fountain flow speeds of $\sim$100 km s^{-1} needed to reproduce the high ion column density ratios and temperatures of $\sim 10^6$ K require $v_{\rm shock} \sim 300$ km s^{-1} (Shapiro & Benjamin 1993; R. Benjamin 1995, private communication). The extreme conditions produced by such a fast shock(s) are likely to completely disrupt grains in the immediate vicinity of the supernovae, as indicated by absorption-line observations of heavy elements in the high-velocity gas (e.g., Jenkins, Wallerstein, & Silk 1984). However, grains swept into the halo by the shock(s) after they have slowed would have a higher probability of surviving. Isotopically anomalous inclusions in meteorites make it clear that some grains can escape supernova explosions and remain intact (Ott 1994).

The recirculation time for gas injected into the halo through a supernova-powered Galactic fountain is on the order of 10^7–10^8 yr depending on the initial gas densities and energy input (Bregman 1980; Tomisaka & Ikeuchi 1986; Mac Low & McCray 1988). Since the dust spends only a portion of this time in the WNM where destructive processing is greatest, it seems possible that resilient grain cores surviving their initial injection into the halo could account for the abundance pattern of the halo clouds. The gas-phase abundance differences seen in Figure 6 as a function of $|z|$ fit a scenario in which grains located at higher z-distances may be exposed to more severe or more frequent shocks than those that are not elevated to large distances from the plane, but even the high-z grain cores avoid destruction by these shocks.

A possible means for elevating diffuse, dusty clouds into the low halo without severe grain disruption is through radiation pressure from stars in the Galactic plane (Franco et al. 1991). This is a physically different method for dust transfer to high-z than discussed above, but it could account for the enhanced scale heights inferred for some refractory elements if grain-gas drag operates to liberate grains into the hotter medium where they become subject to thermal sputtering (see Ferrara et al. 1989). A low-temperature fountain of the type described by Houck & Bregman (1990) to explain the intermediate- and high-velocity cloud system of the Galaxy would also be less destructive than the one responsible for highly ionized gas located several kiloparsecs from the plane. The existence of one or both of these "quiescent" transfer mechanisms would help to explain the z-dependence of the halo could abundance patterns in Table 6 and Figure 6.

There has been a recent suggestion by Lipman & Pettini (1995) based on measurements of interstellar Ti II that dust grains in the low halo are destroyed within a distance of 1 kpc from the Galactic plane. Our observations show that in the halo clouds studied dust destruction is far from complete, and observations of Ti II in the halo clouds toward HD 93521 and μ Col have subsolar gas-phase abundances similar to Ni (see Table 6). We suspect that the difference between the Lipman & Pettini result and ours arises because they measured *total* (disk + halo) Ti II column densities toward the stars in their sample and assumed a single-component exponential density distribution for the gas. Perhaps the rapid return of Ti to the gas traced by their measurements, and which they extrapolate to larger z-distances, is caused by the stripping of grain mantles. We would expect mantle destruction to occur at relatively low z-distances based upon our finding that the dust grains in the halo clouds consist mainly of resilient core material.

Murthy, Walker, & Henry (1992) have shown that broadband (*IRAS*) infrared dust emission near stars at high Galactic latitudes has a more uniform spatial distribution than dust in the Galactic disk. They determine an exponential scale height of about 540 pc for the dust around the most luminous stars in their entire sample but find that about 20% of the objects with $500 \leq |z| \leq 1000$ pc have some dust emission nearby. Although they tentatively identify the dusty regions with the warm ionized medium (WIM) in the McKee & Ostriker (1977) model of the ISM,[8] a subset of this higher z dusty cloud population appears to have properties similar to the warm neutral medium traced by our absorption-line measurements. Ultraviolet spectroscopic investigations of the ions studied in this paper toward halo stars showing IR emission might prove useful in testing this hypothesis.

[8] In the McKee & Ostriker 1977 three-component model of the ISM, the WIM occurs in the ionized envelopes around WNM regions.

8. SUMMARY POINTS

1. We have obtained GHRS observations of the interstellar Mg II, P II, Si II, S II, Mn II, Cr II, Fe II, Ni II, Zn II, and Ge II absorption lines toward HD 116852, a halo star at $z = -1.3$ kpc and $d = 4.8$ kpc in the direction $l = 304.^\circ9$, $b = -16.^\circ1$. The intermediate-resolution (FWHM $\approx$ 11–18 km s^{-1}) observations of these species have S/N $\approx$ 30–90. Our high-resolution (FWHM $\approx$ 3.5 km s^{-1}) observations of Mn II and Fe II have S/N $\approx$ 35.

2. The GHRS measurements and high-resolution Ca II spectra reveal a rich interstellar absorption-line velocity structure extending from ≈ -70 to $+35$ km s^{-1}. The absorption-line profile shapes are strongly affected by differential Galactic rotation, which has a velocity gradient of ≈ -10 km s^{-1} kpc^{-1} in the direction of HD 116852. We study the abundances in two groups of halo clouds:

group 2: $-35 \leq v_{\rm LSR} \leq -10$ km s^{-1};
$0.7 \leq d \leq 2.7$ kpc; $-0.7 \leq z \leq -0.2$ kpc,

group 3: $-70 \leq v_{\rm LSR} \leq -35$ km s^{-1};
$2.7 \leq d \leq 4.8$ kpc; $-1.3 \leq z \leq -0.7$ kpc.

The absorption components within these groups are probably associated with halo gas situated below the Sagittarius-Carina spiral arm (group 2) and Norma-Centaurus spiral arm (group 3).

3. The gas-phase abundances of Mg, Si, S, Mn, Cr, Fe, and Ni relative to Zn in the HD 116852 halo clouds are closer to solar than they are for diffuse cloud sight lines in the disk and are very similar to those found for halo clouds toward high-latitude stars in the solar neighborhood. *There is no systematic dependence on Galactocentric distance in the halo cloud gas-phase abundances (relative to Zn) for $R_g \approx 7$–10 kpc.*

4. Our previous study of the sight line showed that highly ionized gas absorbs at velocities similar to those of the halo clouds studied. *We have considered the effects of a diffuse radiation field on the inferred abundances and find that they should be accurate to $\lesssim$0.15 dex, even if most of the absorption arises in a diffuse gas of the type seen by Reynolds (1993). The abundances are probably accurate to $\lesssim$0.06 dex for a realistic distribution of neutral and ionized gases along the sight line.*

5. Using these gas-phase abundances, we have derived dust-phase abundances of Mg, Si, S, Mn, Cr, Fe, and Ni in the halo clouds. We find that approximately 70% of the Mg, 45% of the Si, and 77% of the Fe atoms in the clouds are locked into dust grains. *The very small variations in the halo cloud abundances strongly support the idea that the cores of the dust grains are resilient and have a basic composition common to widely separated Galactic regions.*

6. We calculate (Mg + Fe)/Si = 3.26 $\pm$ 0.64 or (Mg + Fe)/Si = 3.91 $\pm$ 0.64 in the dust grains if solar or B-star reference abundances are used, respectively. A pure silicate (pyroxene – olibine) grain core having a ratio of 1.0–2.0 may still be possible if the oscillator strengths of the Mg II λ1240 doublet need to be revised and solar abundances are adopted. Without such a revision, or if B-star reference abundances are adopted, *the observed ratios imply that there must be grains composed of Fe-oxides, or perhaps pure Fe, in the halo clouds.*

7. The transfer of dust into the halo may occur through supernova injection or photolevitation of diffuse clouds in the

disk. The gas- and dust-phase abundance patterns in the diffuse halo clouds are consistent with a more severe shocking of the clouds at greater distances from the plane. *Since pure Fe grains are destroyed much more repidly than silicates behind fast shocks, we favor oxides as the additional Fe-bearing material in the halo cloud dust grains.*

We are indebted to John Mathis for making the results of several detailed ionization models of the DIG available to us for this study and for providing helpful comments that improved the manuscript. We also thank Ed Jenkins for providing useful suggestions for several sections of the paper. K. R. S. acknowledges support from a Hubble Fellowship provided by NASA through grant number HF-1038.01-92A from the Space Telescope Science Institute, which is operated by AURA under NASA contract NAS5-26555. B. D. S. recognizes support from NASA grant NAG5-1852.

REFERENCES

Anders, E., & Grevesse, N. 1989, Geochim. Cosmochim. Acta, 53, 197
Arendt, R. G., Dwek, E., & Leisawitz, D. 1992, ApJ, 400, 562
Arendt, R. G., Dwek, E., Petre, R., Dickel, J. R., & Roger, R. S. 1990, ApJ, 350, 266
Bergeson, S. D., & Lawler, J. E. 1993, ApJ, 408, 382
Bok, B. J. 1971, in Highlights in Astronomy, Vol. 2, ed. C. deJager (Washington: GPO)
Brandt, J., et al. 1994, PASP, 106, 890
Bergman, J. N. 1980, ApJ, 236, 577
Buss, R. H., Jr., Allen, M., McCandliss, S., Kruk, J., Liu, J.-C., & Brown, T. 1994, ApJ, 430, 630
Cardelli, J. A., Ebbets, D., & Savage, B. D. 1993, ApJ, 413, 401
Cardelli, J. A., & Savage, B. D. 1995, ApJ, 452, 275
Cardelli, J. A., Savage, B. D., Bruhweiler, F. C., Smith, A. M., Ebbets, D. C., & Sembach, K. R. 1991, ApJ, 420, L29
Cardelli, J. A., Savage, B. D., Sofia, U. J., Keenan, F. P., & Dufton, P. L. 1994, ApJ, 420, L29
Cardelli, J. A., Sembach, K. R., & Savage, B. D. 1995, ApJ, 440, 241
Clemens, D. P. 1985, ApJ, 295, 422
Colomb, F. R., Gil, M., & Morras, R. 1976, A&AS, 26, 195
Courtès, G. 1972, Vistas Astron., 14, 81
Courtès, G., Georgelin, Y. P., Georgelin, Y. M., & Monet, G. 1970, in IAU Symp. 38, The Spiral Structure of Our Galaxy, ed. W. Becker & G. Contopoulos (Dordrecht: Reidel), 209
Dame, T., et al. 1987, ApJ, 322, 708
Danly, L. 1989, ApJ, 342, 785
Diplas, A., & Savage, B. D. 1994, ApJS, 93, 211
Dömgorgen, H., & Mathis, J. S. 1994, J. S. 1994, ApJ, 428, 647
Draine, B. T., & McKee, C. F. 1993, ARA&A, 31, 373
Draine, B. T., & Salpeter, E. E. 1979, ApJ, 231, 438
Dufton, P. L., Hibbert, A., Kingston, A. E., & Tully, J. A. 1983, MNRAS, 202, 145
Dufton, P. L., Keenan, F. P., Hibbert, A., Ojha, P. C., & Stafford, R. P. 1992, ApJ, 387, 414
Dwek, E., & Arendt, R. G. 1992, ARA&A, 30, 11
Dyson, J. E., & Hartquist, T. W. 1983, MNRAS, 203, 1323
Edgar, R. J., Sanders, W. T., Juda, M., McCammon, D., & Kraushaar, W. L. 1993, BAAS, 25, 1461
Edgar, R. J., & Savage, B. D. 1989, ApJ, 340, 762
Fadeyev, Y. 1988, in Atmospheric Diagnostics of Stellar Evolution, ed. K. Nomoto (Berlin: Springer-Verlag), 533
Falgarone, E., & Lequeux, J. 1973, A&A, 25, 253
Ferrara, A., Franco, J., Ferrini, F., & Barsella, B. 1989, in IAU Colloq. 120, Structure and Dynamics of the Interstellar Medium, ed. G. Tenorio-Tagle, M. Moles, & J. Melnick (Berlin: Springer-Verlag), 54
Fitzsimmons, A., Brown, P. J. F., Dufton, P. L., & Lennon, D. J. 1990, A&A, 232, 437
Franco, J., Ferrini, F., Ferrara, A., & Barsella, B. 1991, ApJ, 366, 443
Gies, D. R., & Lambert, D. L. 1992, ApJ, 387, 673
Grossman, L. 1975, Sci. Am., 232, 30
Harris, A. W., & Mas Hesse, J. M. 1986, ApJ, 308, 240
Houck, J., & Bregman, J. N. 1990, ApJ, 352, 506
Jenkins, E. B. 1987, in Interstellar Processes, ed. D. Hollenbach & H. A. Thronson (Dordrecht: Reidel), 533
Jenkins, E. B., Savage, B. D., & Spitzer, L., Jr. 1986, ApJ, 301, 355
Jenkins, E. B., Wallerstein, G. W., & Silk, J. 1984, ApJ, 278, 649
Jones, A. P., Tielens, A. G. G. M., McKee, C. F., & Hollenbach, D. J. 1994, ApJ, 433, 797
Keenan, F. P. 1986, QJRAS, 33, 325
Kerr, F. J., Bowers, P. F., Jackson, P. D., & Kerr, M. 1986, A&AS, 66, 373
Kilian-Motenbruck, J., Gehren, T., & Nissen, P. E. 1994, A&A, 291, 757
Little, J. E., Dufton, P. L., Keenan, F. P., & Conlon, E. S. 1994, ApJ, 427, 267
Lipman, K., & Pettini, M. 1995, ApJ, 442, 628
Lockman, F. J. 1984, ApJ, 283, 90
Lockman, F. J., & Gehman, C. S. 1991, ApJ, 382, 182
Mac Low, M.-M., & McCray, R. 1988, ApJ, 324, 776
McKee, C. F. 1989, in Interstellar Dust, ed. L. J. Allamandola & A. G. G. M. Tielens (Dordrecht: Kluwer), 431
———. 1993, in Back to the Galaxy, ed. S. Holt & F. Verter (New York: AIP), 431
McKee, C. F., Hollenbach, D. J., Seab, C. G., & Tielens, A. G. G. M. 1987, ApJ, 318, 674
McKee, C. F., & Ostriker, J. P. 1977, ApJ, 218, 148
Mihalas, D., & Binney, J. 1981, Galactic Astronomy (2d ed.; San Francisco: Freeman)
Miller, W. W., & Cox, D. P. 1993, ApJ, 417, 579
Moore, C. E. 1970, Ionization Potentials and Ionization Limits Derived from the Analysis of Optical Spectra (Washington, DC: US Dept. of Commerce Report No. NSRDS-NBS 34)
Morton, D. C. 1991, ApJS, 77, 119
Murthy, J., Walker, H. J., & Henry, R. C. 1992, ApJ, 401, 574
Neff, S. G., et al. 1994, ApJ, 430, 545
Nuth, J. A., & Hecht, J. H. 1990, Ap&SS, 163, 79
Ossenkopf, V., Henning, Th., & Mathis, J. S. 1992, A&A, 261, 567
Ott, U. 1994, Nature, 364, 25
Pettini, M., Boksenberg, A., Bates, B., McCaughan, R. F., & McKeith, C. D. 1977, A&A, 61, 839
Rana, N. C. 1991, ARA&A, 29, 129
Reynolds, R. J. 1991, in IAU Symp. 144, The Interstellar Disk-Halo Connection in Galaxies, ed. H. Bloemen (Dordrecht: Kluwer), 67
Reynolds, R. J. 1993, in Back to the Galaxy, ed. S. Holt & F. Verter (New York: AIP), 156
Rickard, J. J. 1974, A&A, 31, 47
Savage, B. D., Bohlin, R. C., Drake, J. F., & Budich, W. 1977, ApJ, 216, 291
Savage, B. D., Cardelli, J. A., & Sofia, U. J. 1992, ApJ, 401, 706
Savage, B. D., Lu, L., Weymann, R., Morris, S., & Gilland, R. 1993, ApJ, 404, 124
Savage, B. D., & Sembach, K. R. 1991, ApJ, 379, 245
———. 1994, ApJ, 434, 145
———. 1995, in preparation
Savage, B. D., Sembach, K. R., & Cardelli, J. A. 1994, ApJ, 420, 183
Seab, C. G., & Shull, J. M. 1983, ApJ, 275, 652
Sembach, K. R. 1994, ApJ, 434, 244
———. 1995, ApJ, 445, 314
Sembach, K. R., & Danks, A. C. 1994, A&A, 289, 539
Sembach, K. R., Danks, A., & Savage, B. D. 1993, A&AS, 100,107
Sembach, K. R., & Savage, B. D. 1992, ApJS, 83, 147
———. 1994, ApJ, 431, 201 (Paper I)
Sembach, K. R., Steidel, C. C., Macke, R. J., & Meyer, D. M. 1995, ApJ, 445, L27
Shapiro, P. R., & Benjamin, R. A. 1993, in Star Forming Galaxies and Their Interstellar Media, ed. J. J. Franco (New York: Cambridge Univ. Press), 273
Shaver, P. A., McGee, R. X., Newton, L. M., Danks, A. C., & Pottasch, S. R. 1983, MNRAS, 204, 53
Sofia, U. J., Cardelli, J. A., & Savage, B. D. 1994, ApJ, 430, 650
Sofia, U. J., Savage, B. D., & Cardelli, J. A. 1993, ApJ, 413, 251
Spitzer, L. 1978, Physical Processes in the Interstellar Medium (New York: Wiley)
Spitzer, L., Jr. 1990, ARA&A, 28, 71
Spitzer, L., Jr., & Fitzpatrick, E. L. 1992, ApJ, 291, L41
———. 1993, ApJ, 409, 299
———. 1995, ApJ, 445, 196
Sutherland, R. S., & Dopita, M. A. 1993, ApJS, 88, 253
Tielens, A. G. G. M., McKee, C. F., Seab, C. G., & Hollenbach, D. J. 1994, ApJ, 431, 321
Tomisaka, K., & Ikeuchi, S. 1986, PASJ, 38, 697
Vancura, O., Raymond, J. C., Dwek, E., Blair, W. P., Long, K. S., & Foster, S. 1994, ApJ, 431, 188
van Steenberg, M. E., & Shull, J. M. 1988, ApJ, 330, 492
Wheeler, J. C., Sneden, C., & Truran, J. W. 1989, ARA&A, 27, 279
Zaritsky, D. 1994, AJ, 108, 1619